Mechanism of stabilization of porous coatings on unstable supersonic mode in hypersonic boundary layers

Tiehan Long (龙铁汉)[1], Ying Dong (董颖)[2], Rui Zhao (赵瑞),[2,a)] and Chihyung Wen(温志湧)[1]

[1]*The Hong Kong Polytechnic University, Kowloon, Hong Kong Special Administrative Region*

[2]*School of Aerospace Engineering, Beijing Institute of Technology, Beijing 100081, China*

This study clarifies the fundamental mechanism by which porous coatings suppress the supersonic mode instability in the hypersonic boundary layer (BL) by using Doak's momentum potential theory. The independent energy budget equations for vortical, acoustic, and thermal components of instabilities are derived. Data from direct numerical simulations of Mach 6.0 flat plate flows on a solid wall and porous coatings are then analyzed. By decomposing the momentum density into vortical, acoustic, and thermal components, the source terms and fluxes are studied based on their corresponding energy corollaries. The results demonstrate the role of different components in the generation and transport of the total fluctuation enthalpy (TFE), and the way in which the fluctuation energy is transferred between components. In the case of the solid wall, the oscillating disturbance on the BL consists of acoustic and vortical components. Near the critical layer, the positive acoustic source and energy transferred from the vortical component are primary energy producers for acoustic fluxes. Then, the TFE is transported outward by the acoustic component, which leads to "sound radiation" in the supersonic mode. In the case of the porous coating, the positive vortical source near the surface of the plate is suppressed significantly. Less vortical energy is transported to the critical layer and thus less vortical energy is transformed into acoustic energy. Acoustic energy is eventually exhausted due to energy loss in the outward transport of the TFE and "sound radiation" disappears from the porous coating.

[a)] Electronic mail: zr@bit.edu.cn

I. INTRODUCTION

The surface of hypersonic vehicles is often subjected to intense aerodynamic heating, and the use of thermal protection systems (TPS) is necessary to protect such vehicles from burning out. The transition to turbulent flow causes a significant increase in the rate of heat transfer, which is a critical challenge in the design of the TPS. Thus, understanding the transition mechanism in the hypersonic boundary layer (BL) is important for the design of high-performance hypersonic vehicles. The primary path to turbulence in a high-speed BL in low-disturbance environments is the modal growth of instability waves,[1,2] and the problem of stabilization has been widely studied by performing wind tunnel experiments,[3–8] linear stability theory (LST) analyses,[9–13] and direct numerical simulations (DNS).[14–18] Mack's second mode becomes dominant in a two-dimensional (2D) BL over adiabatic surfaces for Mach > 4.[2,13] In general, in a BL over an adiabatic wall, a sonic line is present at y_{s1}, where $\bar{M}(y_{s1}) = \frac{\bar{u}(y_{s1})-c}{\bar{a}(y_{s1})} = -1$. Here, $\bar{u}$ is the mean velocity, c is the disturbance phase speed, and $\bar{a}$ is the local sound speed.[9,13] The disturbances travel subsonically above the sonic line but supersonically between the wall and the sonic line as trapped sound waves. Outside the BL, the subsonic wave diminishes exponentially.

Bitter and Shepher[19] studied Mack's second mode by considering the high-level wall cooling effect. The wall-to-edge temperature ratio was $T_w/T_e < 1$, which corresponds to the state obtained in certain high-enthalpy wind tunnel experiments and real flight cases. They found that a special supersonic mode emerged at the edge of the BL and traveled outside it. Inside the BL over a highly cooled wall, another sonic line appeared, where $\bar{M}(y_{s2}) = \frac{\bar{u}(y_{s2})-c}{\bar{a}(y_{s2})} = 1$ above the first sonic line. The disturbance traveled subsonically between these sonic lines, but supersonically above the upper sonic line (along the edge of the BL) and below the lower sonic line. The disturbance reflected between the lower sonic line and the wall as trapped sound waves, similar to that in the case of an adiabatic wall. The supersonic mode was oscillatory outside the BL.[19–23] Notably, Mack's second mode along the edge of the BL transformed from a subsonic mode to a supersonic mode, and the free-stream slow sound waves and Mack's second mode exhibited synchronicity. This supersonic mode broadens the unstable frequency band for disturbance in the flow field.[19] Chuvakhov and Fedorov[20] called this supersonic mode the "spontaneous radiation of sound," which emphasizes the oscillatory disturbance of the supersonic mode outside the BL. Owing to the lower amplification rate of this mode compared with that of Mack's subsonic second mode, the supersonic mode is considered to be insignificant in the transition of the high-speed BL. However, Mortensen[24] recently reported that the rate of growth of the supersonic mode exceeds that of Mack's subsonic second mode in a Mach 20 flow over highly blunt cones. As Mack's second mode exhibits acoustic-wavelike behavior, a straightforward way to suppress its excitation is to dissipate the acoustic wave energy by applying a porous coating,[25-32] which yields the required dissipation effect through the thermal and viscous boundary layers inside the coating's narrow cavities or pores. There is a reasonable prospect that the porous coating can also stabilize the supersonic mode because of its similar acoustic characteristics. This is verified and clarified in this work.

The LST analyses indicate that the supersonic mode is caused due to synchronization of Mack's second mode and slow sound waves in the freestream.[19-23] However, it does not provide a physical

interpretation to the "sound radiation" phenomenon in the supersonic mode. Kuelh, J. proposed a thermoacoustic interpretation of Mack's second-mode instability by considering a Lagrangian cycle-averaged disturbance acoustic energy equation with the inviscid approximation.[33] The physical origins of Mack's second mode energy are attributed to the thermoacoustic Reynolds stress and thermodynamic work.[33] Similarly, Doak's momentum potential theory (MPT)[35] approach is adopted in this work to study the energy source which drives the "sound radiation" in the supersonic mode from an energy perspective. Compared to Kuelh, J.'s Lagrangian approach, Doak's MPT approach includes the viscous effect in the flow field and is applicable to the DNS results immediately.

Note that the above description of the supersonic mode as a "spontaneous radiation of sound" has not been rigorously validated in realistic circumstances. The difficulty pertains to the lack of a universal definition of an "acoustic" or "sound" wave in a high-speed BL that exhibits a strong gradient in the mean flow field. For a compressible, viscous, and heat-conductive uniform flow field, Kovásznauy[34] proposed a split theorem to decompose random fluctuations into three modes, namely, the vortical, entropic, and acoustic modes. In the linear stage, these three modes obey three independent governing equations, and the interactions among them can be ignored. However, Kovásznauy's approach is not applicable to a nonuniform flow field. Doak's MPT[35,36] approach provides an elegant tool for decomposing a time-stationary fluctuation flow field into three components, and overcomes the restriction of Kovásznauy's approach in inhomogeneous systems. In Doak's approach, the momentum density field, $\boldsymbol{m}(\equiv\rho\boldsymbol{u})$, is decomposed into the corresponding vortical, acoustic, and thermal components. Furthermore, an energy corollary for the total fluctuating enthalpy (TFE) is derived. This energy corollary helps define the generation and transport of the TFE in the flow field, which provides a causal interpretation of the development of the disturbances. Unnikrishnan and Gaitonde[37] applied Doak's approach to decompose the instability modes in the BL flow field at Mach 6.0, which they referred to as fluid thermodynamic (FT) decomposition. Specifically, discrete modes in the LST and DNS results of linear and nonlinear saturated disturbances were decomposed into different components. A ropelike pattern was observed in the contour of the vortical component, and a waveguide structure was produced in both the acoustic and entropic components. The mechanisms of the TFE source were studied by considering the instantaneous axial distribution of various source terms in the vicinity of amplification of Mack's second mode. Unnikrishnan and Gaitonde[38] performed FT decomposition of instability waves in the Mach 6 flat plate boundary layer at different wall temperatures. They showed that oscillatory waves outside the highly cooled BL were mostly composed of vortical and acoustic fluctuations. The net outward acoustic flux of the supersonic modes increased with higher levels of wall cooling, as did the perturbation in the wall pressure. Their inspirational work revealed an alternative approach to using the MPT method to study hypersonic BL instabilities. It should be noted that the original definitions of the flux and source terms in Doak's energy corollary are expressed in mean form.[35,36] The quantitative change in the instantaneous flux terms cannot be attributed directly to the instantaneous source terms owing to an additional time-derivative term. The instantaneous energy consideration in Ref. 37 was unsatisfactory in explaining how the fluctuation energy changes owing to various sources. Also, the possible radiation mechanisms in the supersonic mode are difficult to fully clarify without considering the mean source terms.[39]

This work analyzes the mean source and flux terms based on Doak's energy corollary, with the aim of explaining how porous coatings stabilize the supersonic mode in a highly cooled BL. After numerically simulating the flow field, the DNS results are decomposed into different components according to Doak's MPT approach. Then, the various mean source and flux terms are compared to

study the mechanism of the source of the supersonic mode in the case of a solid wall and a porous coating. Physical interpretations of the stabilization phenomena are obtained under Doak's MPT framework.

II. METHODOLOGY

A. Direct numerical simulation

In this study, the DNS method used in the authors' earlier work[29,40] was adopted. The 2D Navier–Stokes equations in the conservation form consist of a mass conservation equation, two momentum conservation equations, and an energy conservation equation. The dimensional governing equation in an arbitrary curvilinear coordinate system $(\xi,\ \eta)$ can be expressed as

$$\frac{\partial \boldsymbol{Q}}{\partial t}+\frac{\partial \boldsymbol{E}}{\partial \xi}+\frac{\partial \boldsymbol{F}}{\partial \eta}=0. \tag{1}$$

Here, $\boldsymbol{Q}$ is a vector of the conservative variables, and $\boldsymbol{E}$ and $\boldsymbol{F}$ denote flux vectors in the ξ and η directions, respectively. The curvilinear coordinate system $(\xi,\ \eta)$ is mapped into the Cartesian coordinate system $(x,\ y)$. Thus, these vectors are restated in terms of the corresponding vectors $\boldsymbol{Q}_c$, $\boldsymbol{E}_c$, and $\boldsymbol{F}_c$ in the Cartesian coordinate system as

$$\boldsymbol{Q}=J\boldsymbol{Q}_c, \boldsymbol{E}=J\left(\boldsymbol{E}_c\frac{\partial \xi}{\partial x}+\boldsymbol{F}_c\frac{\partial \xi}{\partial y}\right), \boldsymbol{F}=J\left(\boldsymbol{E}_c\frac{\partial \eta}{\partial x}+\boldsymbol{F}_c\frac{\partial \eta}{\partial y}\right). \tag{2}$$

Here, the transformation Jacobian J is defined as $J=\left|\frac{\partial(x,y)}{\partial(\xi,\eta)}\right|$. The Cartesian vectors are defined as

$$\boldsymbol{Q}_c=\begin{Bmatrix}\rho\\ \rho u\\ \rho v\\ e\end{Bmatrix}, \boldsymbol{E}_c=\begin{Bmatrix}\rho u\\ \rho u^2+p-\tau_{xx}\\ \rho uv-\tau_{xy}\\ u(e+p)-u\tau_{xx}-v\tau_{xy}+q_x\end{Bmatrix}, \boldsymbol{F}_c=\begin{Bmatrix}\rho v\\ \rho uv-\tau_{xy}\\ \rho v^2+p-\tau_{yy}\\ v(e+p)-u\tau_{xy}-v\tau_{yy}+q_y\end{Bmatrix}. \tag{3}$$

Here, ρ is density, u and v denote the components of velocity in Cartesian coordinates, $e=\frac{p}{\gamma-1}+\frac{\rho(u^2+v^2)}{2}$ is the specific total energy, and p is pressure. The stress tensor τ and heat flux q are defined as

$$\tau_{xx}=2\mu\frac{\partial u}{\partial x}-\frac{2}{3}\mu\left(\frac{\partial u}{\partial x}+\frac{\partial v}{\partial y}\right),\qquad \tau_{xy}=\mu\left(\frac{\partial u}{\partial y}+\frac{\partial v}{\partial x}\right),\qquad \tau_{yy}=2\mu\frac{\partial v}{\partial y}-\frac{2}{3}\mu\left(\frac{\partial u}{\partial x}+\frac{\partial v}{\partial y}\right). \tag{4}$$

$$q_x=-k\frac{\partial T}{\partial x},\qquad q_y=-k\frac{\partial T}{\partial y}, \tag{5}$$

where T is the temperature. The perfect gas condition was assumed, with the specific heat ratio $\gamma=1.4$ and Prandtl number $Pr=0.72$. The dynamic viscosity coefficient μ and heat conductivity k were determined according to Sutherland's law.

A high-order, accurate, shock-fitting finite difference method was used to solve the governing equations numerically. The inviscid flux derivatives were discretized using the fifth-order upwind compact scheme while the viscous terms were discretized using a sixth central difference scheme. A third-order Runge–Kutta method was applied for temporal integration. This method has been successfully applied to study the effects of the local temperature[40] and porous coatings[29] in the context of the stability of hypersonic BL. Two numerical simulations were performed for Mach 6.0 BL flows on a solid wall and a porous coating. The flow conditions were set to be similar to those used in Refs.

20 and 38. In both cases, the freestream Mach number M_∞ was 6.0, and the unit Reynolds number was 1×10^7 m^{-1}. The freestream temperature and wall temperature were 300 K and 150 K, respectively. The length of the flat plate was $L = 0.6$ m, and the computational domain was extended from $x = 0\,m$ to $x = -0.02\,m$. The symmetry condition was adopted between $x = -0.02\,m$ and $x = 0\,m$ at $y = 0$ for numerical robustness. The computational grid had 3607×320 nodes clustered at the leading edge and the plate surface after a grid independence study. In the case of the porous coating, a coating corrugated with subwavelength grooves was placed at $x = 0.3$ m– 0.6 m, and was modeled by the wall boundary condition $v'=p'/Z$. The surface impedance Z took into account high-order diffracted modes with the formulation[29]

$$Z = \rho_w c_w + \frac{\rho_w c_w}{jtan(k_c H)\phi(\rho_w/\tilde{\rho})(k_c/k_0)} - \sum_{n=-\infty}^{+\infty} \frac{\rho_w c_w k_0}{\sqrt{k_0^2 - \left(\frac{2\pi n}{s}\right)^2}} S_n^2 . \tag{6}$$

Here, the parameters of the coating were the same as in Ref. 31, with porosity $\phi = 0.76$, depth $H = 1.64\times10^{-3}$m, and half-width $b = 1.96\times10^{-4}$ m. The other parameters in Eq. (6) can be found in Ref. 31.

After steady-state calculations, a slot of periodic suction–blowing perturbation was introduced to the basic flow at the leading edge.

$$q_w(x,t) = \varepsilon\sin\left(2\pi\frac{x-x_1}{x_2-x_1}\right)\sin(2\pi f t), \quad x_1 \le x \le x_2. \tag{7}$$

Here, q_w is the normal mass flow rate, $x_1 = 0.03$ m, and $x_2 = 0.045$ m. The force amplitude ε =0.001 was adopted to ensure the small disturbance assumption. The forcing frequency f was fixed at 495 kHz for both cases, and at this frequency, the supersonic mode was speculated to excite at $x >$ 0.34m [20].

B. Momentum potential theory

To clarify the context, Doak's MPT[35,36] is summarized as follows: The momentum density $\boldsymbol{m}$ was selected as the primary dependent vector field to be decomposed. According to the Helmholtz theorem, the vector field $\boldsymbol{m}$ can be split into its rotational component $\boldsymbol{m}_B$ and an irrotational component. The latter can be expressed as a gradient of a scalar potential ψ.

$$\boldsymbol{m} \equiv \rho\boldsymbol{u} = \boldsymbol{m}_B - \nabla\psi, \quad \nabla\cdot\boldsymbol{m}_B = 0. \tag{8}$$

For a time-stationary flow field, each instantaneous flow quantity consists of a mean part and a fluctuation part:

$$\bar{\boldsymbol{m}} = \bar{\boldsymbol{m}}_B - \nabla\bar{\psi}, \quad \boldsymbol{m}' = \boldsymbol{m}_B' - \nabla\psi'. \tag{9}$$

The mean continuity equation and the fluctuation continuity equation can be expressed as follows:

$$\nabla\cdot\bar{\boldsymbol{m}} = 0, \qquad \frac{\partial\rho'}{\partial t} + \nabla\cdot\boldsymbol{m}' = 0. \tag{10}$$

The mean momentum density $\bar{\boldsymbol{m}}$ is divergence free. By substituting the corresponding Eq. (9) into Eq. (10), the mean scalar potential $\bar{\psi}$ can be assumed to be zero, and a Poisson equation is obtained for the scalar potential of fluctuation:

$$\frac{\partial\rho'}{\partial t} = \nabla^2\psi'. \tag{11}$$

For a single-chemical-component continuum in the thermal equilibrium state, the density ρ can be defined as a function of the thermodynamic pressure p and entropy S:

$$\rho = \rho(p,S). \tag{12}$$

Consequently,

$$\frac{\partial \rho'}{\partial t} = \frac{\partial \rho}{\partial p}\frac{\partial p'}{\partial t} + \frac{\partial \rho}{\partial S}\frac{\partial S'}{\partial t}, \qquad \frac{\partial \rho}{\partial p} = \frac{1}{a^2} = \frac{1}{\gamma RT}, \qquad \frac{\partial \rho}{\partial S} = -\frac{(\gamma-1)\rho}{\gamma R}. \tag{13}$$

Hence, the scalar potential ψ' can be assumed to be a linear superposition of an acoustic potential ψ'_A and a thermal potential ψ'_T:

$$\psi' = \psi'_A + \psi'_T, \qquad \frac{1}{\gamma RT}\frac{\partial p'}{\partial t} = \nabla^2\psi'_A, \qquad -\frac{(\gamma-1)\rho}{\gamma R}\frac{\partial S'}{\partial t} = \nabla^2\psi'_T. \tag{14}$$

The fluctuation momentum density $\boldsymbol{m}'$ is expressed as a superposition of the vortical component $\boldsymbol{m}'_B$, acoustic component $\boldsymbol{m}'_A$, and thermal component $\boldsymbol{m}'_T$.

$$\boldsymbol{m}' = \boldsymbol{m}'_B + \boldsymbol{m}'_A + \boldsymbol{m}'_T, \qquad \boldsymbol{m}_A{}' = -\nabla\psi'_A, \qquad \boldsymbol{m}_T{}' = -\nabla\psi'_T. \tag{15}$$

In this study, the Poisson equations for ψ' and ψ'_A were solved. Subsequently, ψ'_T and $\boldsymbol{m}'_B$ were obtained using $\psi' - \psi'_A$ and $\boldsymbol{m}' - \boldsymbol{m}'_A - \boldsymbol{m}'_T$, respectively. The Dirichlet boundary conditions for the Poisson equations were formulated by integration along the boundaries, as in Refs. 37 and 39.

Another critical aspect of Doak's MPT approach is the energy budget for the total fluctuating enthalpy (TFE), $H' = \left(C_p T + \frac{\boldsymbol{u}\cdot\boldsymbol{u}}{2}\right)'$. The mean transport equation of the TFE due to $\boldsymbol{m}'$ can be written as

$$\nabla \cdot \overline{H'\boldsymbol{m}'} = -\overline{\boldsymbol{m}'\cdot\boldsymbol{\alpha}'} + \overline{(\rho T)'\frac{\partial S'}{\partial t}}, \tag{16}$$

where $\overline{H'\boldsymbol{m}'}$ is the mean TFE flux, which represents the TFE transported by $\boldsymbol{m}'$ in a time-stationary process, and the acceleration vector $\boldsymbol{\alpha}'$ is defined as

$$\boldsymbol{\alpha}' = (\boldsymbol{\Omega}\times\boldsymbol{u})' - \left(T\nabla S + \frac{1}{\rho}\nabla\cdot\bar{\bar{\boldsymbol{S}}}\right)', \tag{17}$$

where $\boldsymbol{\Omega}$ and $\bar{\bar{\boldsymbol{S}}}$ denote the vorticity vector and the viscous stress tensor, respectively, $-\overline{\boldsymbol{m}'\cdot\boldsymbol{\alpha}'}$ is the rate of production or dissipation of the TFE per unit volume due to the interaction between $\boldsymbol{m}'$ and $\boldsymbol{\alpha}'$, and $\overline{(\rho T)'\frac{\partial S'}{\partial t}}$ represents the change in fluctuation energy in the thermal diffusion process due to the presence of entropy fluctuation $\frac{\partial S'}{\partial t}$.

The first term in the right-hand side of Eq. (17) is the fluctuation Lamb vector $(\boldsymbol{\Omega}\times\boldsymbol{u})'$, which represents the effect of vorticity fluctuations. The second and third terms account for the effects of the entropy gradient and viscous stresses, respectively. Because the fluctuation momentum density $\boldsymbol{m}'$ is a superposition of the vortical, acoustic, and thermal components, the terms $H'\boldsymbol{m}'$ and $\boldsymbol{m}'\cdot\boldsymbol{\alpha}'$ can be split into different components of energy flux and the source. Substituting Eq. (15) into Eq. (16) yields

$$\nabla\cdot\left[\overline{H'\boldsymbol{m}'_B} + \overline{H'\boldsymbol{m}'_A} + \overline{H'\boldsymbol{m}_T{}'}\right] = -\left[\overline{\boldsymbol{m}'_B\cdot\boldsymbol{\alpha}'} + \overline{\boldsymbol{m}'_A\cdot\boldsymbol{\alpha}'} + \overline{\boldsymbol{m}_T{}'\cdot\boldsymbol{\alpha}'}\right] + \overline{(\rho T)'\frac{\partial S'}{\partial t}}. \tag{18}$$

The left-hand-side terms in Eq. (18) are terms of the energy flux that represent the fluctuation energy transported by different components of flow. The first three terms on the right-hand side indicate the various sources of the interaction of the vector α' with different components. In addition to the source terms due to the MPT components, a dissipative source term, $\overline{(\rho T)'\frac{\partial S'}{\partial t}}$, exists due to the irreversible process.

However, the effects of different source terms on different energy flux terms are ambiguous in Eq. (18). In this study, three independent mean transport equations of the TFE due to each component were

derived to clarify the contribution of the source terms to each energy flux term.

The relation between the fluctuation velocity $\boldsymbol{u}'$ and the fluctuation momentum density is

$$\boldsymbol{m}'_B + \boldsymbol{m}'_A + \boldsymbol{m}'_T = \bar{\rho}\boldsymbol{u}' + \overline{\boldsymbol{u}}\left(\frac{\partial \rho}{\partial p}p' + \frac{\partial \rho}{\partial S}S'\right). \tag{19}$$

Thus, $\boldsymbol{u}'$ can be decomposed into its vortical, acoustic, and thermal components as well

$$\boldsymbol{u}' = \boldsymbol{u}'_B + \boldsymbol{u}'_A + \boldsymbol{u}'_T, \qquad \boldsymbol{m}'_B = \bar{\rho}\boldsymbol{u}'_B, \qquad \boldsymbol{m}'_A = \bar{\rho}\boldsymbol{u}'_A + \frac{\overline{\boldsymbol{u}}}{\gamma R\overline{T}}p', \qquad \boldsymbol{m}'_T = \bar{\rho}\boldsymbol{u}'_T - \frac{(\gamma-1)\bar{\rho}\overline{\boldsymbol{u}}}{\gamma R}S'. \tag{20}$$

The linearized momentum equation can be expressed as

$$\frac{\partial \boldsymbol{u}'}{\partial t} + \nabla H' = -\boldsymbol{\alpha}'. \tag{21}$$

The desired expression of each energy budget equation can be obtained by the scalar product of Eq. (21) and the corresponding components of fluctuation momentum density. The derivation of the acoustic energy budget equation is presented here as an example. The scalar product of Eq. (21) and $\boldsymbol{m}'_A$ gives

$$\boldsymbol{m}'_A \cdot \frac{\partial \boldsymbol{u}'}{\partial t} + \boldsymbol{m}'_A \cdot \nabla H' = -\boldsymbol{m}'_A \cdot \boldsymbol{\alpha}'. \tag{22}$$

Considering Eqs. (14) and (20), Eq. (22) can be expressed as

$$\frac{\partial}{\partial t}(\boldsymbol{m}'_A \cdot \boldsymbol{u}') - \boldsymbol{u}' \cdot \frac{\partial}{\partial t}\left(\bar{\rho}\boldsymbol{u}'_A + \frac{\overline{\boldsymbol{u}}}{\gamma R\overline{T}}p'\right) + \nabla \cdot (\boldsymbol{m}'_A H') + \left(\frac{p'}{\bar{\rho}} + \overline{T}S' + \overline{\boldsymbol{u}} \cdot \boldsymbol{u}'\right)\frac{1}{\gamma R\overline{T}}\frac{\partial p'}{\partial t} = -\boldsymbol{m}_A{}' \cdot \boldsymbol{\alpha}'. \tag{23}$$

The time average of Eq. (23) gives the acoustic energy budget equation as

$$\nabla \cdot \left(\overline{\boldsymbol{m}'_A H'}\right) = -\overline{\boldsymbol{m}'_A \cdot \boldsymbol{\alpha}'} + \bar{\rho}\overline{\boldsymbol{u}'_B \cdot \frac{\partial \boldsymbol{u}'_A}{\partial t}} + \bar{\rho}\overline{\boldsymbol{u}'_T \cdot \frac{\partial \boldsymbol{u}'_A}{\partial t}} - \frac{1}{\gamma R}\overline{S'\frac{\partial p'}{\partial t}}. \tag{24}$$

Similarly, we obtain the vortical and thermal energy budget equations as

$$\nabla \cdot \left(\overline{\boldsymbol{m}'_B H'}\right) = -\overline{\boldsymbol{m}'_B \cdot \boldsymbol{\alpha}'} + \bar{\rho}\overline{\boldsymbol{u}'_A \cdot \frac{\partial \boldsymbol{u}'_B}{\partial t}} + \bar{\rho}\overline{\boldsymbol{u}'_T \cdot \frac{\partial \boldsymbol{u}'_B}{\partial t}}, \tag{25}$$

$$\nabla \cdot \left(\overline{\boldsymbol{m}'_T H'}\right) = -\overline{\boldsymbol{m}'_T \cdot \boldsymbol{\alpha}'} + \bar{\rho}\overline{\boldsymbol{u}'_B \cdot \frac{\partial \boldsymbol{u}'_T}{\partial t}} + \bar{\rho}\overline{\boldsymbol{u}'_A \cdot \frac{\partial \boldsymbol{u}'_T}{\partial t}} + \frac{\gamma-1}{\gamma R}\overline{p'\frac{\partial S'}{\partial t}}. \tag{26}$$

The left-hand side of Eqs. (24), (25), and (26) contain only the mean transport of the TFE due to the corresponding component of momentum density. The first terms on the right-hand side of Eqs. (24), (25), and (26) are the source terms due to the corresponding component. The second and third terms satisfy the condition

$$\overline{\boldsymbol{u}'_B \cdot \frac{\partial \boldsymbol{u}'_A}{\partial t}} + \overline{\boldsymbol{u}'_A \cdot \frac{\partial \boldsymbol{u}'_B}{\partial t}} = 0, \qquad \overline{\boldsymbol{u}'_T \cdot \frac{\partial \boldsymbol{u}'_A}{\partial t}} + \overline{\boldsymbol{u}'_A \cdot \frac{\partial \boldsymbol{u}'_T}{\partial t}} = 0, \qquad \overline{\boldsymbol{u}'_B \cdot \frac{\partial \boldsymbol{u}'_T}{\partial t}} + \overline{\boldsymbol{u}'_T \cdot \frac{\partial \boldsymbol{u}'_B}{\partial t}} = 0. \tag{27}$$

Thus, these terms are the energy exchange terms between components. In Eqs. (24) and (26) there are source terms due to the interaction between fluctuation pressure p' and fluctuation entropy S'. The sum of these two terms gives $\overline{\frac{p'}{R}\frac{\partial S'}{\partial t}}$, from which the source term $\overline{(\rho T)'\frac{\partial S'}{\partial t}}$ is extracted due to thermal diffusion in Eq. (18). The sum of Eqs. (24), (25), and (26) gives Eq. (18). First, Eqs. (24), (25), and (26) clarify that the source term due to each component influences only the flux of the TFE due to the corresponding component; a positive source means that the fluctuation energy is extracted from the mean flow to strengthen the transport of the TFE and a negative source implies that the fluctuation energy sinks into the mean flow. Second, the energy exchange term between any pair of components is confirmed to be $\bar{\rho}\overline{\boldsymbol{u}'_a \cdot \frac{\partial \boldsymbol{u}'_b}{\partial t}}$. Third, the interaction between fluctuation pressure p' and fluctuation entropy S' due to thermal diffusion affects the mean transport of the TFE by $\boldsymbol{m}'_A$ and $\boldsymbol{m}'_T$.

III. RESULTS AND DISCUSSION

A. Linear stability results

With the small disturbance and local parallel assumption, the spatial linear stability analysis is conducted for the solid wall case with the same flow condition and the same blow-suction frequency as in the DNS calculation. In the spatial LST, the flow quantity ϕ is assumed to be

$$\phi = \bar{\phi} + \phi', \phi' = \hat{\phi}(y)e^{i(\alpha x - \omega t)} \tag{28}$$

Here, $\bar{\phi}$ is the mean quantity and ϕ' is the fluctuation quantity; $\alpha = \alpha_r + i\alpha_i$ is the (complex) streamwise wave number and ω is the (real) circular frequency. The spatial growth rate is $\sigma = -\alpha_i$ and the phase speed is $c_{ph} = \frac{\omega}{\alpha_r}$. There are two discrete modes in the LST eigenmodes: the fast mode (F mode) and the slow mode (S mode)[41]. In this highly cooled wall case, Mack's second mode is the F mode instead of the S mode in the adiabatic wall case[Error! Bookmark not defined.19,20]. The trajectory in the $(\frac{c_{ph}}{u_\infty}, \sigma)$ plane are shown in FIG. 1, respectively. Three vertical dashed lines in FIG. 1(a) on the left (red), center (blue), and right (green) indicate the location $(1 - 1/M_\infty)$, 1, and $(1 + 1/M_\infty)$, which correspond to slow sound waves, vorticity/entropy waves, and fast sound waves in the freestream, respectively. Arrows in FIG. 1 represent the trend in $\frac{c_{ph}}{u_\infty}$ of the F mode as x increases. The F mode originates from fast sound waves is stable ($\sigma < 0$). Then, the F mode synchronizes with vorticity/entropy waves and becomes unstable ($\sigma > 0$) after cross vorticity/entropy waves. Finally, the F mode coalesces with slow sound waves and leads to the supersonic mode and a new stable mode. The LST result of the solid wall case is consistent well with the results of Ref. 19 and Ref. 20.

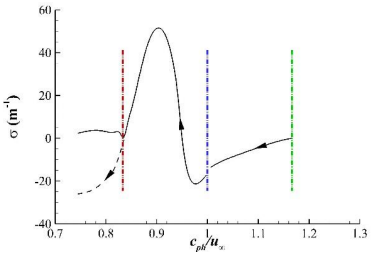

FIG. 1. The trajectory of the F mode in the $(\frac{c_{ph}}{u_\infty}, \sigma)$ plane. The dashed line shows the new stable mode. Here, u_∞ is the free stream velocity.

B. DNS results

An instantaneous snapshot of p', $(\rho u)'$ and $(\rho v)'$ from the results of the DNS of the solid wall and the porous coating are shown in the left column and the right column of FIG. 2, respectively.

In the solid wall case, the fluctuations induced by the suction/blowing actuator were bifurcated into two regions, one aligning along the shock wave and the other traveling downstream within the boundary layer. An unstable supersonic mode occurred at x~$0.34m$, and p', $(\rho u)'$, and $(\rho v)'$ were not evanescent above the BL. The so-called region of "spontaneous sound radiation"[20] is enlarged as the perturbations propagated downstream, and it appears as though they were radiating outward at a

fixed degree. In general, the peak values of fluctuations in the streamwise momentum [FIG. 2 (b1, b2)] were an order of magnitude higher than those of the wall-normal component [FIG. 2 (c1, c2)].

In contrast to the case of the solid wall, when the disturbances traveled downstream through the porous coating ($x = 0.3 - 0.6$ m), there was no visible "spontaneous sound radiation" phenomenon [FIG. 2 (a2)]. The fluctuations within the BL were significantly suppressed, and this indicates that the porous coatings could effectively suppress the amplification of Mack's second mode and the supersonic mode.

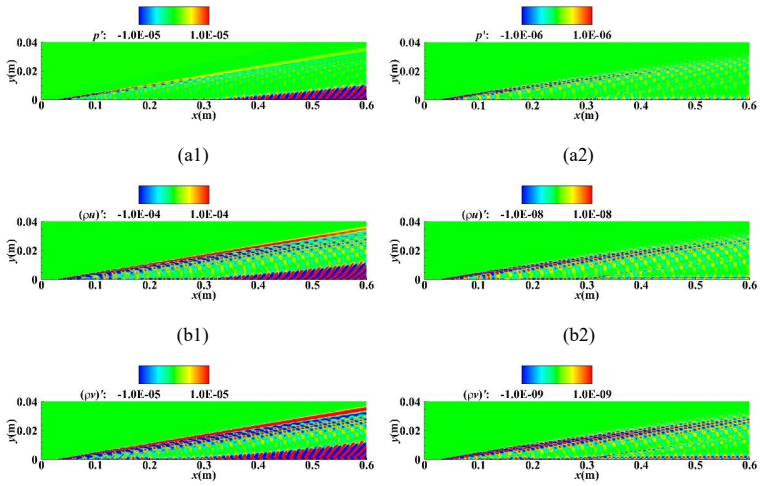

FIG. 2. Instantaneous snapshots of (a1, a2) p' (Pa), (b1, b2) $(\rho u)'$ (kg/m^2/s), and (c1, c2) $(\rho v)'$ (kg/m^2/s) in the case of the solid wall (left column) and the porous wall (right column).

C. MPT decomposition

The different components were extracted by applying Doak's MPT approach to the instantaneous fluctuation field. An instantaneous snapshot of the magnitudes of the vortical component ($\|\boldsymbol{m}_B'\|$), acoustic component ($\|\boldsymbol{m}_A'\|$), and thermal component ($\|\boldsymbol{m}_T'\|$) of the solid wall and the porous wall are depicted in the left column and the right column of FIG. 3, respectively.

In the solid wall case, the result captures vortical perturbations from small fluctuations induced at the leading shock wave by the blowing–suction actuator of the wall. The vortical and thermal perturbations had the largest and smallest magnitudes, respectively. Both $\boldsymbol{m}_B'$ and $\boldsymbol{m}_A'$ were present in the region of oscillation outside the BL, while the thermal component was not prominent in the "sound radiation." This observation, which agreed well with the result in Ref. 33, indicates that the "sound radiation" was not sufficiently precise to describe the unstable supersonic mode. Both acoustic and vortical waves existed in the "radiation" region.

FIG. 4 shows the distribution of $\|\boldsymbol{m}_B'\|$, $\|\boldsymbol{m}_A'\|$, and $\|\boldsymbol{m}_T'\|$ along the x axis at y=0m in the solid wall case and the porous wall case. On the porous coating, the amplitude of each component was reduced by an order of magnitude at x=0.4m [FIG. 4(a) and FIG. 4(b)]. The effect of the coating end (x = 0.3m), associated with the juncture between the solid and porous parts, induced vortical and slight acoustic components along the expansion wave.[31] The vortical component continued to be the

dominant one in terms of exhibiting the highest amplitude among all FT components [FIG. 3(a2)]. Moreover, the regions of "sound radiation" in the acoustic and vortical components disappeared [FIG. 3(b2) and FIG. 3(c2)].

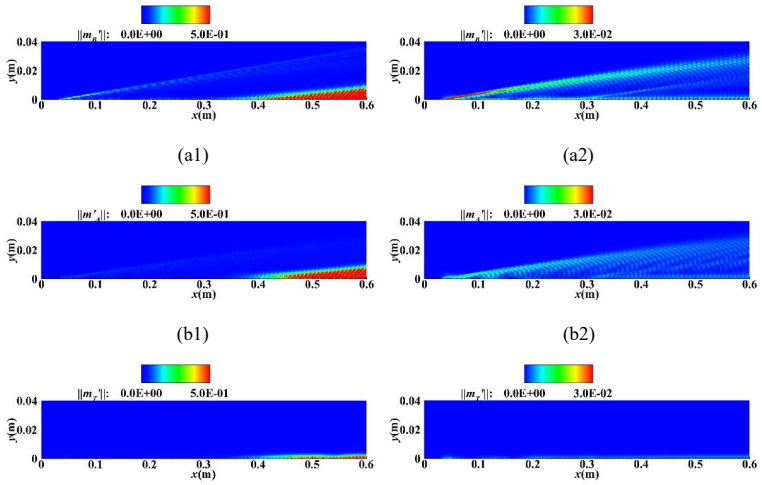

FIG. 3. Magnitudes of (a1, a2) m'_B, (b1, b2) m'_A, and (c1, c2) m'_T in the case of the solid wall (left column) and the porous wall (right column). (unit: kg/(m²•s).

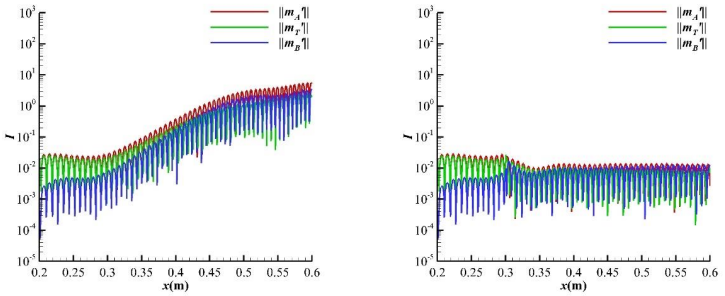

FIG. 4. Magnitudes of m'_B, m'_A, and m'_T at y=0m in the case of the solid wall (left column) and the porous wall (right column). (unit: kg/(m²•s)

D. Mean transport of the TFE

In this section, the mean transport of the TFE by different components of the MPT is discussed to provide insights into the development of perturbations in the BL. For convenience of discussion, the x gradient of the streamwise transport of the TFE, $\frac{\partial}{\partial x}\left(\overline{m'_{Bx}H'}\right)$, $\frac{\partial}{\partial x}\left(\overline{m'_{Ax}H'}\right)$, and $\frac{\partial}{\partial x}\left(\overline{m'_{Tx}H'}\right)$ are denoted by $\boldsymbol{J_{Bx}}$, $\boldsymbol{J_{Ax}}$, and $\boldsymbol{J_{Tx}}$, respectively. Similarly, the y gradient of the normal transport of the TFE,

$\frac{\partial}{\partial y}\left(\overline{m'_{By}H'}\right)$, $\frac{\partial}{\partial y}\left(\overline{m'_{Ay}H'}\right)$, and $\frac{\partial}{\partial y}\left(\overline{m'_{Ty}H'}\right)$ are denoted by $\boldsymbol{J_{By}}$, $\boldsymbol{J_{Ay}}$, and $\boldsymbol{J_{Ty}}$, respectively. The vortical source $-\overline{\boldsymbol{m}'_B \cdot \boldsymbol{\alpha}'}$, acoustic source $-\overline{\boldsymbol{m}'_A \cdot \boldsymbol{\alpha}'}$, and thermal source $-\overline{\boldsymbol{m}'_T \cdot \boldsymbol{\alpha}'}$ are designated as $\boldsymbol{P_B}$, $\boldsymbol{P_A}$, and $\boldsymbol{P_T}$, respectively. The sources due to thermal diffusion $-\frac{1}{\gamma R}\overline{S'\frac{\partial p'}{\partial t}}$ and $\frac{\gamma-1}{\gamma R}\overline{p'\frac{\partial S'}{\partial t}}$ in Eqs. (24) and (26) are respectively designated as $\boldsymbol{P_{diff1}}$ and $\boldsymbol{P_{diff2}}$. The energy exchange from component a to b, $\overline{\bar{\rho}\boldsymbol{u}'_a \cdot \frac{\partial \boldsymbol{u}'_b}{\partial t}}$, is denoted by $\boldsymbol{Ex_{ab}}$. The sums of each of the right-hand-side source terms in Eqs. (24), (25), and (26) are $\boldsymbol{N_A}$, $\boldsymbol{N_B}$, and $\boldsymbol{N_T}$, respectively. Thus, the energy budgets of Eqs. (24), (25), and (26) can be expressed as

$$\boldsymbol{J_{Ax}} + \boldsymbol{J_{Ay}} = \boldsymbol{N_A} = \boldsymbol{P_A} + \boldsymbol{P_{diff1}} + \boldsymbol{Ex_{BA}} + \boldsymbol{Ex_{TA}} \tag{29}$$

$$\boldsymbol{J}_{Bx} + \boldsymbol{J}_{By} = \boldsymbol{N}_B = \boldsymbol{P_B} + \boldsymbol{Ex_{AB}} + \boldsymbol{Ex_{TB}} \tag{30}$$

$$\boldsymbol{J_{Tx}} + \boldsymbol{J_{Ty}} = \boldsymbol{N_T} = \boldsymbol{P_T} + \boldsymbol{P_{diff2}} + \boldsymbol{Ex_{BT}} + \boldsymbol{Ex_{AT}} \tag{31}$$

$\boldsymbol{J_{Ax}}$, $\boldsymbol{J_{Bx}}$, $\boldsymbol{J_{Tx}}$, $\boldsymbol{J_{Ay}}$, $\boldsymbol{J_{By}}$, and $\boldsymbol{J_{Ty}}$ on the solid wall and the porous coating at x = 0.48 m are illustrated in FIG. 5. The magnitudes of $\boldsymbol{J_{Ax}}$, $\boldsymbol{J_{Bx}}$, and $\boldsymbol{J_{Tx}}$ were much smaller than those of $\boldsymbol{J_{Ay}}$, $\boldsymbol{J_{By}}$, and $\boldsymbol{J_{Ty}}$ in the BL. This indicates that the source terms on the right-hand side of Eqs. (29), (30), and (31) influenced the normal transport of the TFE in the first place, possibly because the y gradient of mean flow was much stronger than the x gradient in the BL flow field. In the case of the solid wall, $\boldsymbol{J_{Ay}}$ reached its positive peak at around y_c = 0.001 m (the critical layer where $\bar{M}(y_c) = \frac{\bar{u}(y_c)-c}{\bar{a}(y_c)} = 0$) and then became negative above this peak. This indicates the acoustic source terms strengthened acoustic flux in the y direction at around the critical layer and then weakened it in the negative region. $\boldsymbol{J_{By}}$ had a negative peak at around the critical layer while $\boldsymbol{J_{Ty}}$ was positive between two sonic lines. In the case of the porous wall, the acoustic flux $\boldsymbol{J_{Ay}}$ behaved similarly to that in the case of the solid wall. $\boldsymbol{J_{By}}$ first reached a negative peak and then changed to a positive peak above the critical layer, and $\boldsymbol{J_{Ty}}$ showed a contrary trend to $\boldsymbol{J_{By}}$, but with a slightly smaller magnitude. In the detailed analysis of the source terms provided in the next section, the reversals in $\boldsymbol{J_{By}}$ and $\boldsymbol{J_{Ty}}$ are found to be related to the terms of energy exchange. Notably, the magnitudes of the gradient of TFE fluxes along the solid wall are much larger than that along the porous coating.

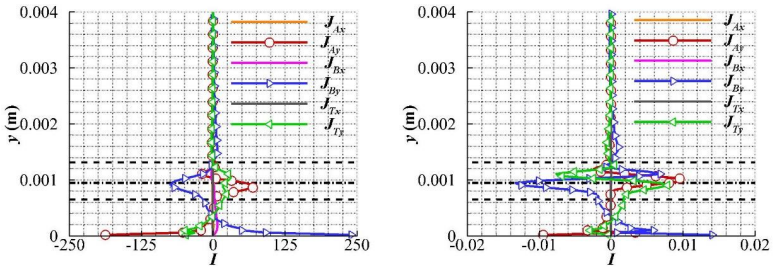

(a) (b)

FIG. 5. Gradients of TFE fluxes at x = 0.48m in the cases of the solid wall (a) and the porous coating (b). The sonic line and critical layer are marked using a dashed line and dash dotted line, respectively (unit: kg/(m•s^3).

FIG. 6 shows the acoustic, vortical, and thermal flux lines in the range of x = 0.45–0.5 m, which

indicates the directions of the mean transport of the TFE according to its respective components in the flow field. The background shows contours of N_A, N_B, and N_T. As is shown in FIG. 6(a1), acoustic fluxes originated at around the critical layer owing to the acoustic source terms and diffused. Above this layer, the TFE was transported toward the bulk flow by m'_A, leading to the "spontaneous sound radiation." In FIG. 6 (b1), the vortical source terms produced energy for the vortical fluxes in the vicinity of the surface of the plate. Then, vortical fluxes originating from the plate's surface sank at the critical layer. The TFE was transported from the bulk flow into the BL by m'_B. Compared with N_A and N_B, the intensity of the thermal source terms was so weak that the thermal component was not prominent in the region of "sound radiation" [FIG. 6(c1) and FIG. 3(c1)]. In the case of the porous coating [FIG. 6(a2)–6(c2)], the sum of the source terms, i.e., N_A, N_B, and N_T, was about four orders of magnitude smaller than that in the case of the solid wall. As is shown in FIG. 6(a2), N_A at around the critical layer was so weak that the upward acoustic flux lines finally turned upward. The TFE was barely transported out of the BL by m'_A. As a result, the "spontaneous radiation phenomenon" was absent in the case of the porous coating.

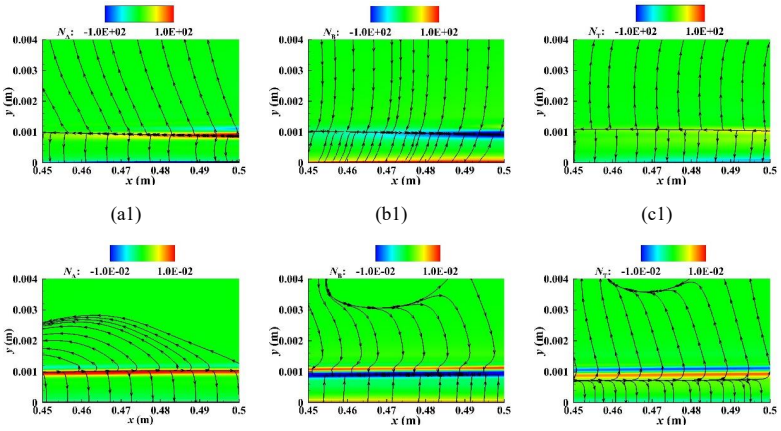

FIG. 6. (a1, a2) acoustic, (b1, b2) vortical, and (c1, c2) thermal fluxes in the cases of the solid wall (upper row) and the porous coating (lower row; unit: kg/(m•s^3).

E. Source mechanisms

FIG. 7 shows the contour of the acoustic source terms and FIG. 8 shows the distribution of the acoustic source terms along the y axis at x=0.48m. The left column represents the case of the solid wall and the right column that of the porous coating. In the former case, P_A was a primary energy producer near the critical layer, and extracted fluctuation energy from the mean flow. Then, P_A dissipated this fluctuation energy during the upward transport of the TFE due to m'_A [FIG. 7(a1)]. P_{diff1} always dissipates the fluctuation energy near the critical layer [FIG. 7(b1)]. The fluctuation energy was transferred from the vortical part to the acoustic part near the critical layer [FIG. 7(c1)], while acoustic fluctuation energy was transferred into thermal energy [FIG. 7(d1)]. The amplitude of Ex_{BA} was larger than that of Ex_{TA}. Therefore, Ex_{BA} compensated for the energy loss due to Ex_{TA} and became the other primary energy producer besides P_A near the critical layer. In this regard, the outward acoustic fluxes and "sound radiation" phenomenon were directly related to P_A and Ex_{BA}. In the case of the porous wall,

the energy exchange terms Ex_{BA} and Ex_{TA} had nearly the same magnitude [FIG. 7(c2) and 7(d2)]. Due to the balance between Ex_{BA} and Ex_{TA}, P_A was the unique primary energy producer in this case [FIG. 7(a2)]. However, P_A was significantly suppressed compared with that in case of the solid wall, and this weakened the outward transport of the TFE by m'_A.

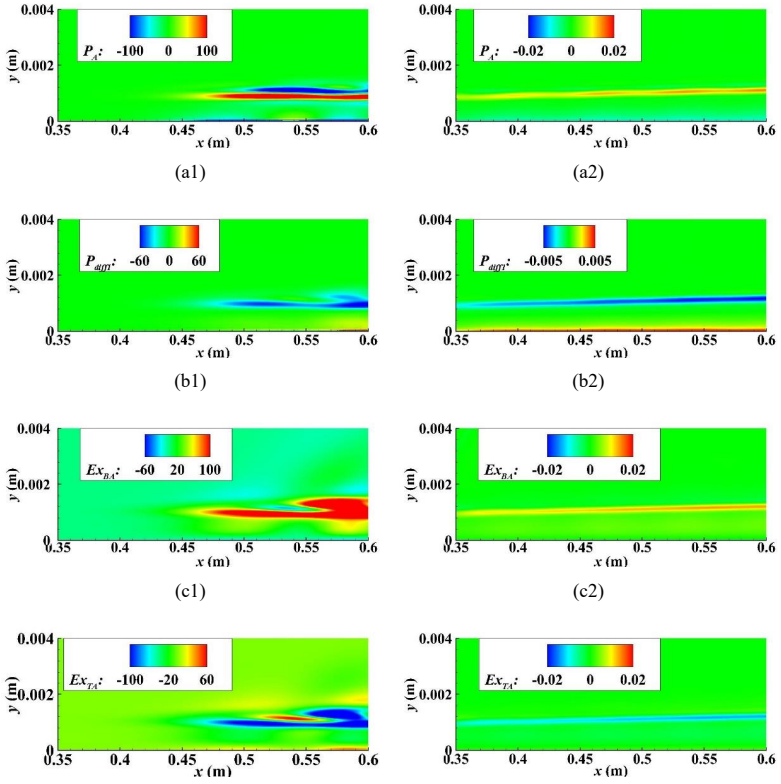

FIG. 7. Left column: acoustic source terms for the solid wall; right column: acoustic source terms for the porous coating (unit: kg/(m•s^3).

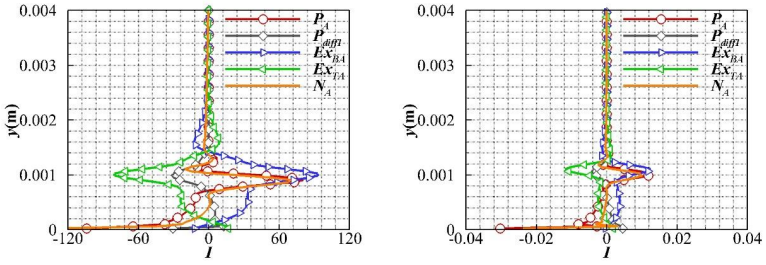

(a) (b)

FIG. 8. Acoustic source terms at x = 0.48m in the cases of the solid wall (a) and the porous coating (b) (unit: kg/(m•s^3).

FIG. 9 shows the contour of vortical source terms and FIG. 10 shows the distribution of the vortical source terms along the y axis at x=0.48m. In the case of the solid wall, $\boldsymbol{P_B}$ was the energy producer in the vicinity of the surface of the plate [FIG. 9(a1)]. Near the critical layer, vortical energy was transformed into acoustic energy [FIG. 9(b1)], which led to a significant sink in the vortical fluxes [FIG. 6(b1)]. In case of the porous wall, $\boldsymbol{P_B}$ was suppressed at the plate's surface and thus less vortical energy was transported to the critical layer. Furthermore, $\boldsymbol{Ex_{TB}}$ had a larger amplitude than $\boldsymbol{Ex_{AB}}$, which was in contrast to the case of the solid wall, and led to reversals in $\boldsymbol{J_{By}}$ and $\boldsymbol{J_{Ty}}$ [FIG. 5(b)].

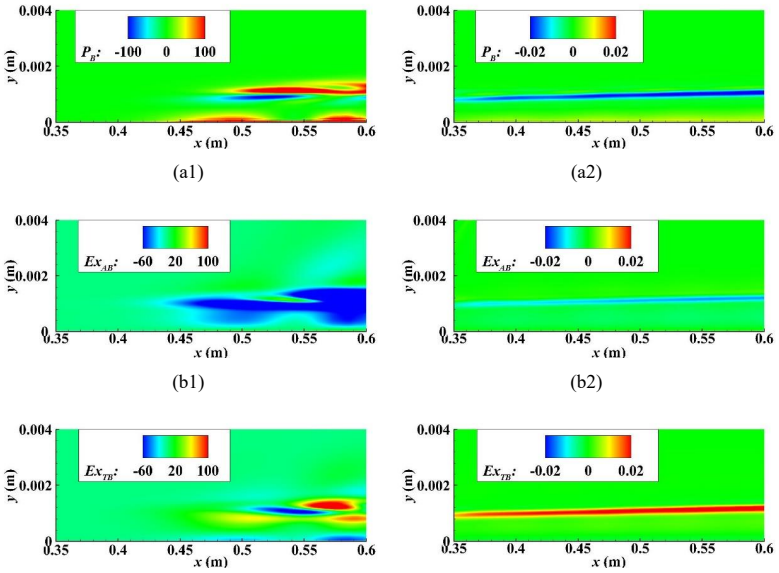

(a1) (a2)

(b1) (b2)

(c1) (c2)

FIG. 9. Left column: vortical source terms for the solid wall; right column: vortical source terms for the porous coating (unit: kg/(m•s^3).

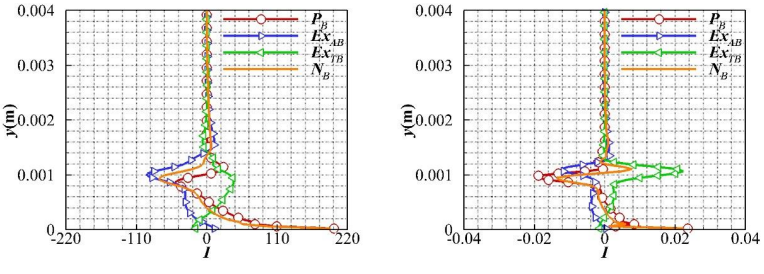

(a) (b)

FIG. 10. Vortical source terms at x = 0.48m in the cases of the solid wall (a) and the porous coating (b) (unit: kg/(m•s^3).

FIG. 11 shows the contour of the thermal source terms and FIG. 12 shows the distribution of the thermal source terms along the y axis at x=0.48m. In the case of the solid wall, $\boldsymbol{Ex_{AT}}$ was the primary energy producer of thermal fluxes, which were transformed from acoustic energy near the critical layer [FIG. 11(c1)]. Nearly all of the energy produced by $\boldsymbol{Ex_{AT}}$ and $\boldsymbol{P_T}$ was consumed by the negative $\boldsymbol{Ex_{BT}}$ and $\boldsymbol{P_{diff2}}$, leading to a marginal value of $\boldsymbol{N_T}$ [FIG. 6(c1)]. Therefore, the thermal component was not prominent in the region of "sound radiation." In the case of the porous wall, $\boldsymbol{P_T}$ was the primary energy producer, and was approximately balanced by the negative $\boldsymbol{Ex_{BT}}$ [FIG. 11 (d2)]. The magnitudes of the source terms on the porous coating were much smaller than those over the solid wall.

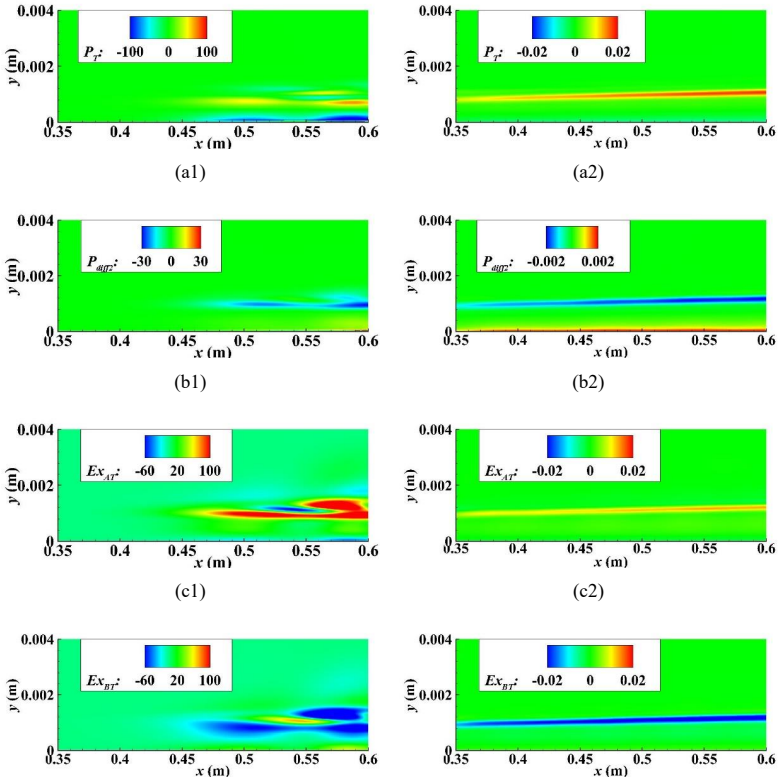

FIG. 11. Left column: vortical source terms for the solid wall; right column: vortical source terms for the porous coating (unit: kg/(m•s^3).

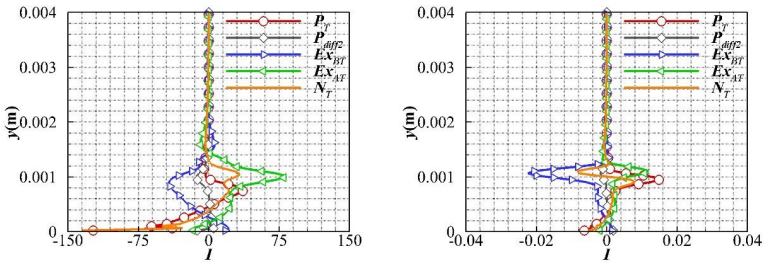

(a) (b)

FIG. 12. Thermal source terms at x = 0.48m in the cases of the solid wall (a) and the porous coating (b) (unit: kg/(m•s^3).

IV. CONCLUSIONS

In this study, the vortical, acoustic, and thermal components were extracted from the results of DNS for hypersonic BLs on a solid wall and a porous coating by using Doak's MPT decomposition. Three independent energy budget equations for each component were derived to clarify the contributions of the source terms to each energy flux term. This approach showed that the normal transport of the TFE by the acoustic component was responsible for the mechanisms of "sound radiation" in the supersonic mode. In the case of the solid wall, the vortical and acoustic components coexisted in the region of radiation of the supersonic mode. P_A and Ex_{BA} near the critical layer produced energy for acoustic fluxes to transport the TFE to the bulk flow, which was responsible for the "sound radiation." P_B produced energy for vortical fluxes in the vicinity of the plate surface. However, vortical fluxes sank near the critical layer and fluctuation energy was transformed from vortical component to the acoustic component. Ex_{AT} and P_T produced energy for thermal fluxes near the critical layer, and then were consumed by Ex_{BT} and P_{diff2}. In the case of the porous coating, P_B in the vicinity of the plate's surface was suppressed, and less vortical energy was transported to the critical layer. Therefore, less vortical energy was transformed into acoustic energy and P_A became the unique energy produced for acoustic fluxes. The energy produced by P_A could not compensate for energy loss during the outward transport of the TFE. Eventually, there was no "spontaneous radiation phenomenon" on the porous coating.

AUTHOR'S CONTRIBUTIONS

The first two authors contributed equally to this work.

ACKNOWLEDGMENTS

The work was carried out at the National Supercomputer Center in Tianjin, and the calculations were performed on the TianHe-1 (A).

AIP PUBLISHING DATA SHARING POLICY

The data that support the findings of this study are available from the corresponding author upon reasonable request.

Appendix: numerical grid verification

The numerical solution was verified by increasing the grid resolution by a factor of $\sqrt{2}$ in each direction (solid wall case). As shown in FIG. 13, the discrepancy is less than 1%, and that suggests the grid independence for simulating the development of disturbance. Therefore, the DNS calculations in this paper are based on the grid resolution of 3607×320 nodes, in order to save computational time.

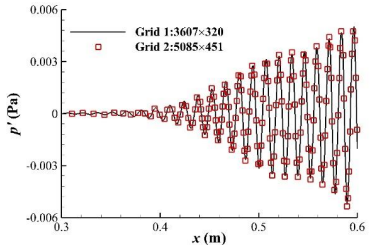

FIG. 13. Numerical grid verification.

REFERENCES

[1]M. Morkovin, E. Reshotko, and T. Herbert, "Transition in open flow systems: a reassessment," Bull. Am. Phys. Soc. **39**, 1882 (1994).

[2]A. V. Fedorov, "Transition and stability of high-speed boundary layers," Annu. Rev. Fluid Mech. **43**, 79–95 (2011).

[3]J. M. Kendall, "Wind tunnel experiments relating to supersonic and hypersonic boundary-layer transition," AIAA J. **13**, 290–299 (1975).

[4]K. F. Stetson, E. R. Thompson, J. C. Donaldson, and L. G. Siler, "Laminar boundary layer stability experiments on a cone at mach 8. part V: Tests with a cooled model," AIAA Paper. 1889–1895 (1989).

[5]A. D. Kosinov, A. A. Maslov, and S. G. Shevelkov, "Experiments on the stability of supersonic laminar boundary layers," J. Fluid Mech. **219**, 621–633 (1990).

[6]K. F. Stetson and R. Kimmel, "On hypersonic boundary-layer stability," AIAA Paper No. 92-737, 1992.

[7]S. J. Laurence, A. Wagner, and K. Hannemann, "Experimental study of second-mode instability

growth and breakdown in a hypersonic boundary layer using high-speed schlieren visualization," J. Fluid Mech. **797**, 471–503 (2016).

[8]R. E. Kennedy, S. J. Laurence, M. S. Smith, and E. C. Marineau, "Visualization of the second-mode instability on a sharp cone at Mach 14," AIAA Paper No. 18-2083, 2018.

[9]L. M. Mack, "Boundary-layer stability theory," Document 900-277, Rev. A. JPL, Pasadena (1969).

[10]L. M. Mack, "Boundary-layer linear stability theory," in *AGARD Conference* (1984). 224, p. 1-1–1-22.

[11]M. R. Malik, "Prediction and control of transition in supersonic and hypersonic boundary layers," AIAA J. **27**, 1487–1493 (1989).

[12]M. R. Malik, "Numerical methods for hypersonic boundary layer stability," J. Comput. Phys. **86**, 376–413 (1990).

[13]H. L. Reed, W. Saric, and D. Arnal, "Linear stability theory applied to boundary layers," Ann. Rev. Fluid Mech. **28**, 389–482 (1996).

[14]G. Erlebacher and M. Y. Hussaini, "Numerical experiments in supersonic boundary ‐ Layer stability," Phys. Fluids A: Fluid Dynamics. **2**, 94–104 (1990).

[15]Y. B. Ma and X. L. Zhong, "Receptivity of a supersonic boundary layer over a flat plate. Part 1. Wave structures and interactions," J. Fluid Mech. **488**, 31–78 (2003).

[16]Y. B. Ma and X. L. Zhong, "Receptivity of a supersonic boundary layer over a flat plate. Part 2. Receptivity to free-stream sound," J. Fluid Mech. **488**, 79–121 (2003)

[17]Y. B. Ma and X. L. Zhong, "Receptivity of a supersonic boundary layer over a flat plate. Part 3. Effects of different types of free-stream disturbances," J. Fluid Mech. **532**, 63–109 (2005).

[18]X. L. Zhong and X. W. Wang, "Direct numerical simulation on the receptivity, instability, and transition of hypersonic boundary layers," Annu. Rev. Fluid Mech. **44**, 527–561 (2012).

[19]N. Bitter and J. Shepherd, "Stability of highly cooled hypervelocity boundary layers," J. Fluid Mech. **778**, 586–620 (2015).

[20]P. V. Chuvakhov and A. V. Fedorov, "Spontaneous radiation of sound by instability of a highly cooled hypersonic boundary layer," J. Fluid Mech. **805**, 188–206 (2016).

[21]C. P. Knisely and X. Zhong, "Significant supersonic modes and the wall temperature effect in hypersonic boundary layers," AIAA J. **57**, 1552–1566 (2018).

[22]C. P. Knisely and X. Zhong, "Sound radiation by supersonic unstable modes in hypersonic blunt cone

boundary layers. I. Linear stability theory," Phys. Fluids **31**, 024103 (2019).

[23]C. P. Knisely and X. Zhong, "Sound radiation by supersonic unstable modes in hypersonic blunt cone boundary layers. II. Direct numerical simulation," Phys. Fluids **31**, 024104 (2019).

[24]C. H. Mortensen, "Toward an understanding of supersonic modes in boundary-layer transition for hypersonic flow over blunt cones," J. Fluid Mech. **846**, 789–814 (2018).

[25]Fedorov, A. V., Malmuth, N. D., Rasheed, A., and Hornung, H. G., "Stabilization of hypersonic boundary layers by porous coatings," AIAA J., **39**, 605-610(2001).

[26]Fedorov, A. V. and Yumashev, D. V., "Theoretical analysis of acoustic instability of a hypersonic shock layer on a porous wall," J. Applied Mech. and Tech. Phys., **46**, 33-41, (2005).

[27]X. W. Wang and X. L. Zhong, "The stabilization of a hypersonic boundary layer using local sections of porous coating," Phys. Fluids **24**, 034105 (2012).

[28]G. A. Brès, M. Inkman, T. Colonius, and A. V. Fedorov, "Second-mode attenuation and cancellation by porous coatings in a high- speed boundary layer," J. Fluid Mech. **726**, 312–337 (2013).

[29]R. Zhao, T. Liu, C. Y. Wen, J. Zhu, and L. Cheng, "Theoretical modeling and optimization of porous coating for hypersonic laminar flow control," AIAA J. **56**, 2942–2946 (2018).

[30]R. Zhao, X. X. Zhang, and C. Y. Wen, "Theoretical modeling of porous coatings with simple microstructures for hypersonic boundary-layer stabilization," AIAA J. **58**, 981–986 (2020).

[31]R. Zhao, C. Y. Wen, T. H. Long, X. D. Tian, L. Zhou, and Y. Wu, "Spatial direct numerical simulation of the hypersonic boundary-layer stabilization using porous coatings," AIAA J. **57**, 5061–5065 (2019).

[32]J. K. Xu, J. X. Liu, S. Mughal, P. X. Yu, and J. Q. Bai, "Secondary instability of Mack mode disturbances in hypersonic boundary layers over micro-porous surface," Phys. Fluids **32**, 044105 (2020).

[33]Kuehl, J., "Thermoacoustic interpretation of second-mode instability," AIAA J. **56**, 3585-3592 (2018)

[34]L. Kovásznauy, "Turbulence in supersonic flow," J. Aeronaut Sci. 20, 657–682 (1953).

[35]P. E. Doak, "Momentum potential theory of energy flux carried by momentum fluctuations," J. sound and Vib. 131, 67–90 (1989).

[36]P. E. Doak, "Fluctuating total enthalpy as the basic generalized acoustic field," Theor. Comput. Fluid Dyn. **10**, 115–133 (1998).

[37]S. Unnikrishnan and D. V. Gaitonde, "Interactions between vortical, acoustic and thermal components during hypersonic transition," J. Fluid Mech. **868**, 611–647 (2019).

[38]S. Unnikrishnan and D. V. Gaitonde, "Instability characteristics of cooled hypersonic boundary layers," AIAA Paper No. 20-0588, 2020.

[39]G. Daviller, P. Comte, and P. Jordan, "Flow decomposition for the study of source mechanisms," AIAA Paper No. 09-3305, 2009.

[40]R. Zhao, C. Y. Wen, X. D. Tian, T. H. Long, and W. Yuan, "Numerical simulation of local wall heating and cooling effect on the stability of a hypersonic boundary layer," Int. J. Heat Mass Transf. **121**, 986–998 (2018).

[41]Fedorov, A., and Tumin, A., "High-speed boundary-layer instability: old terminology and a new framework," AIAA J.**49**, 1647-1657(2011).

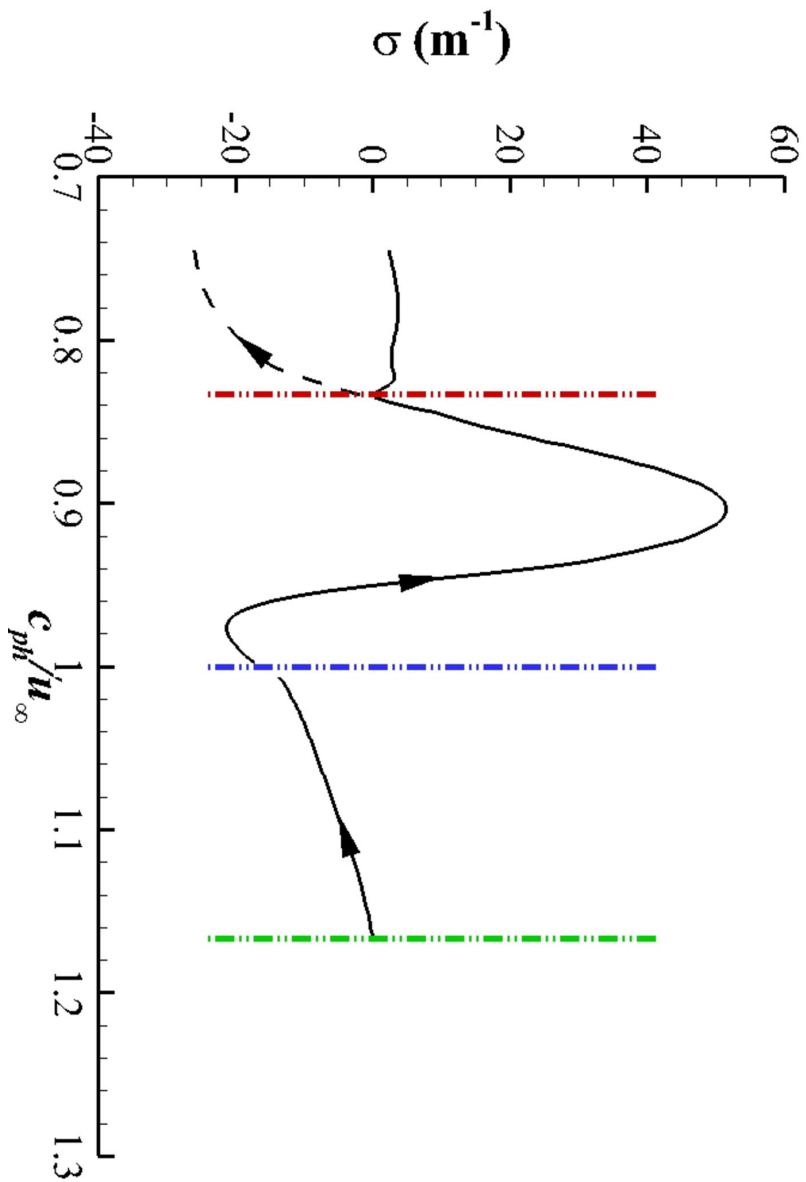

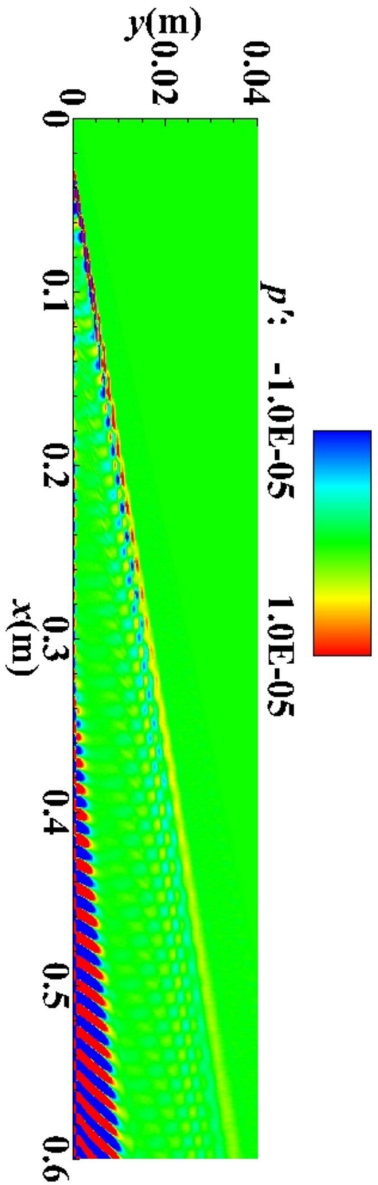

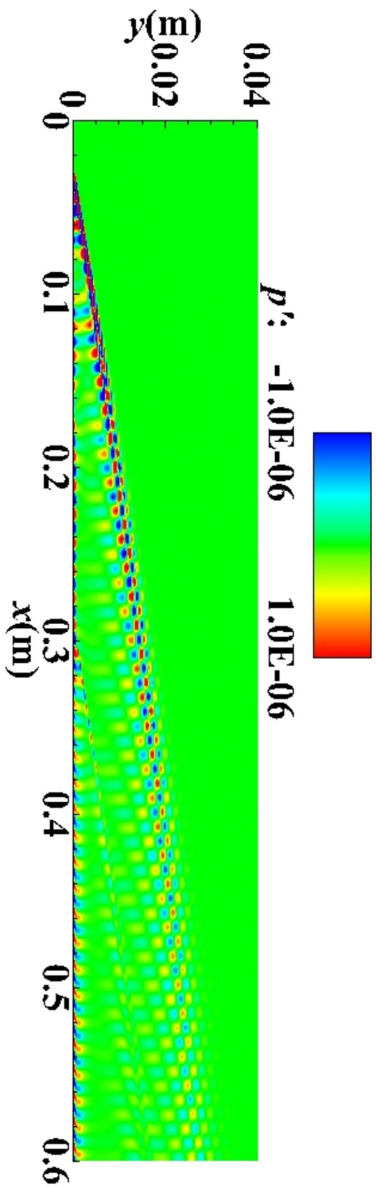

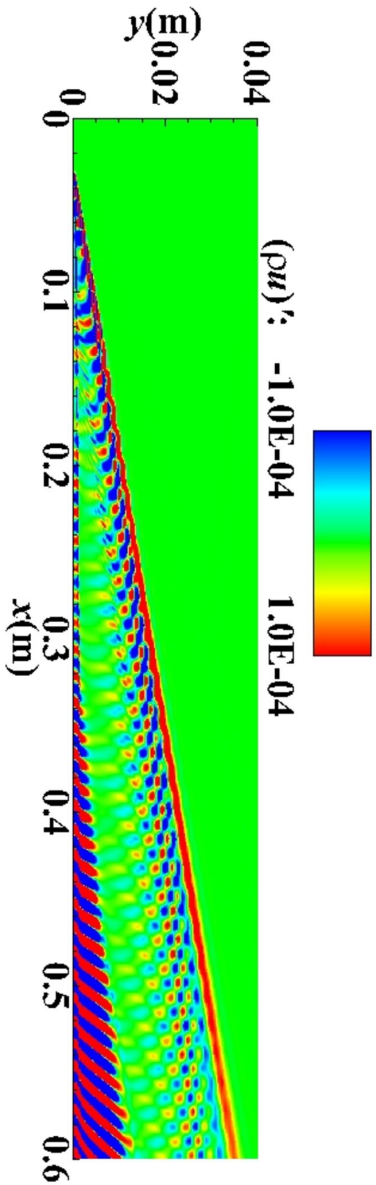

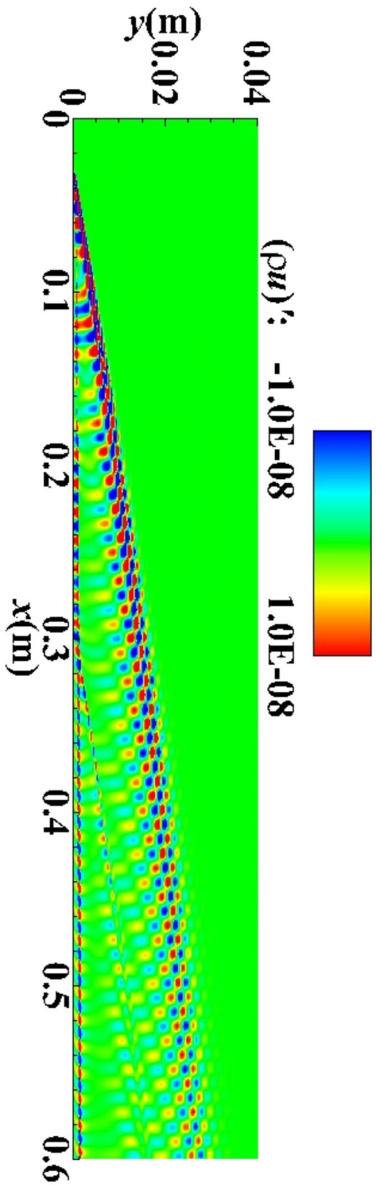

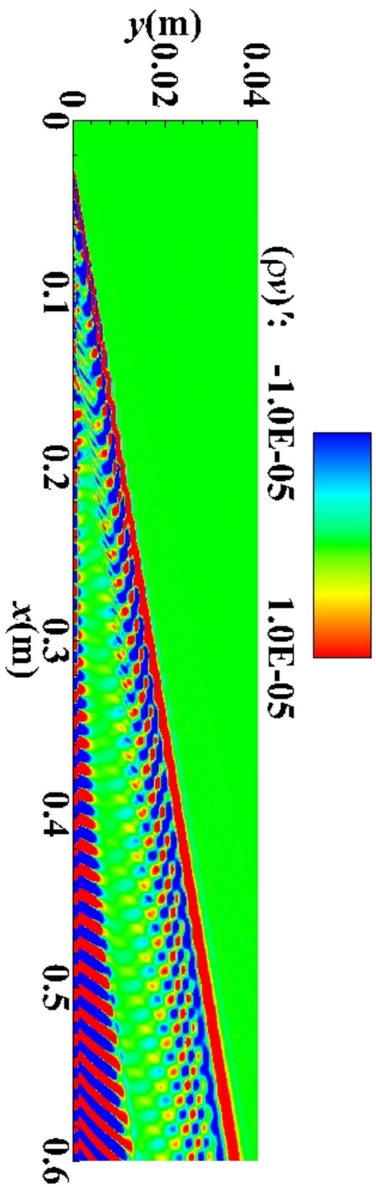

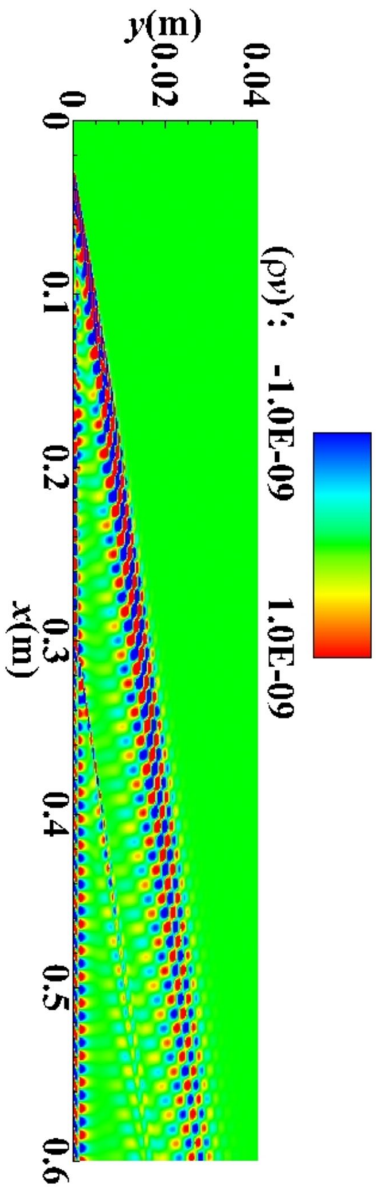

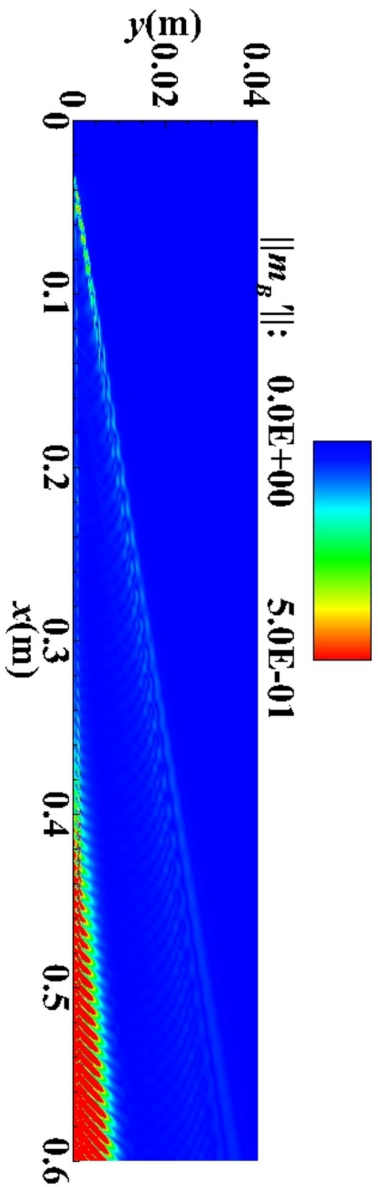

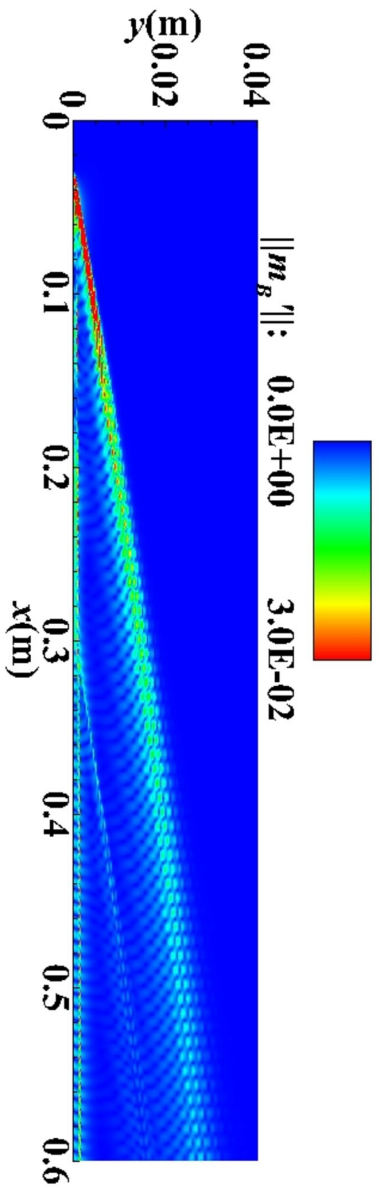

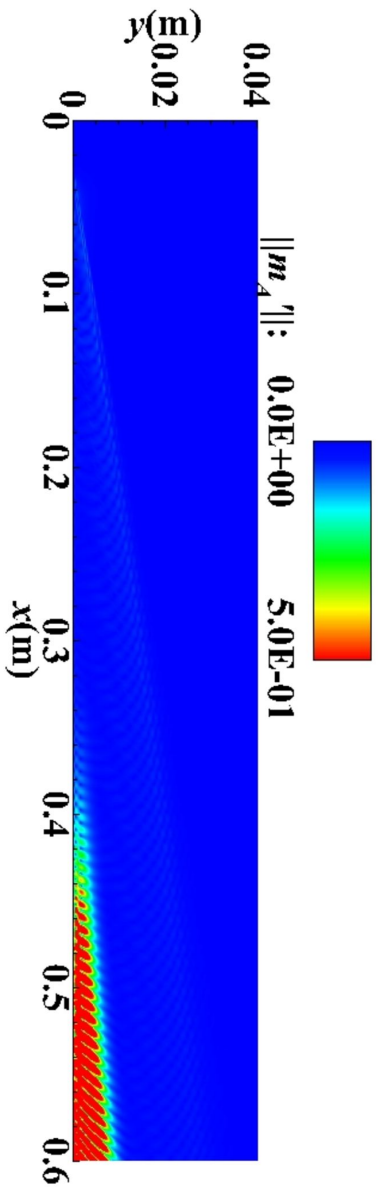

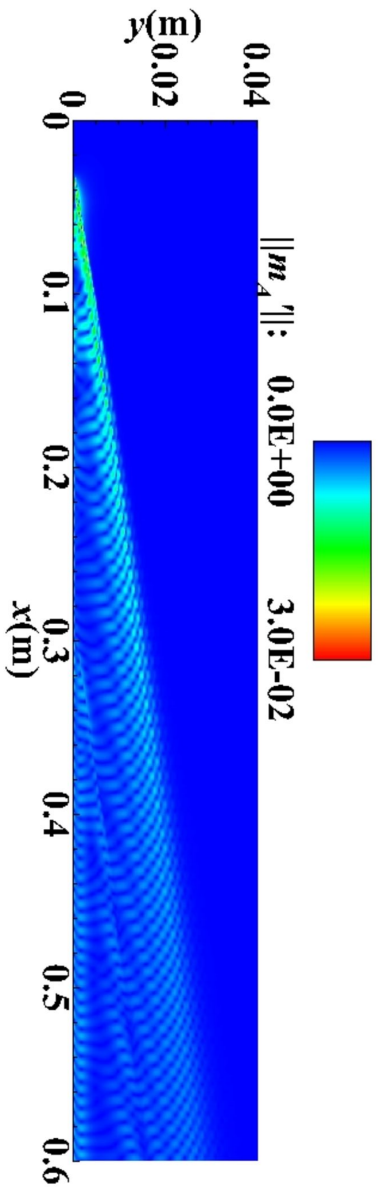

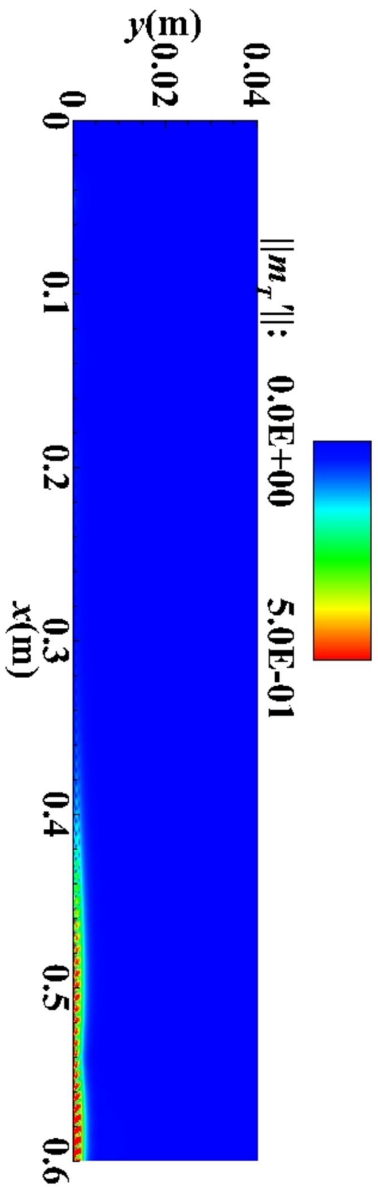

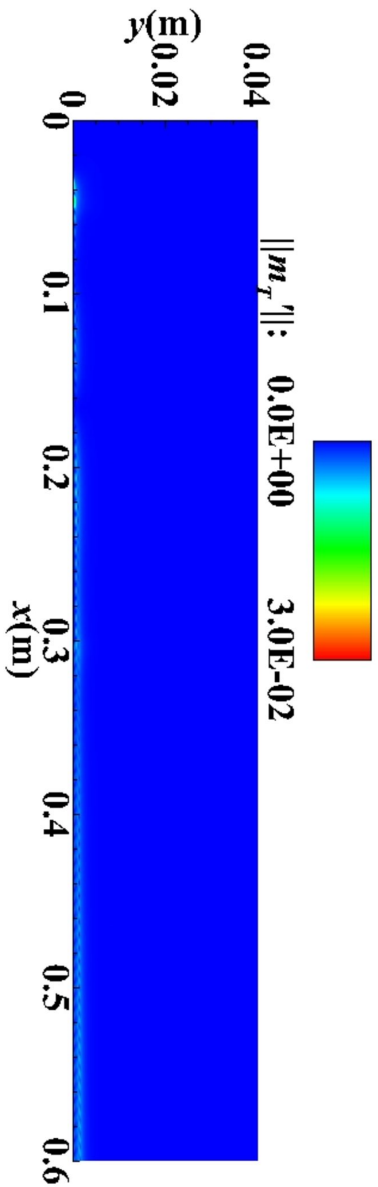

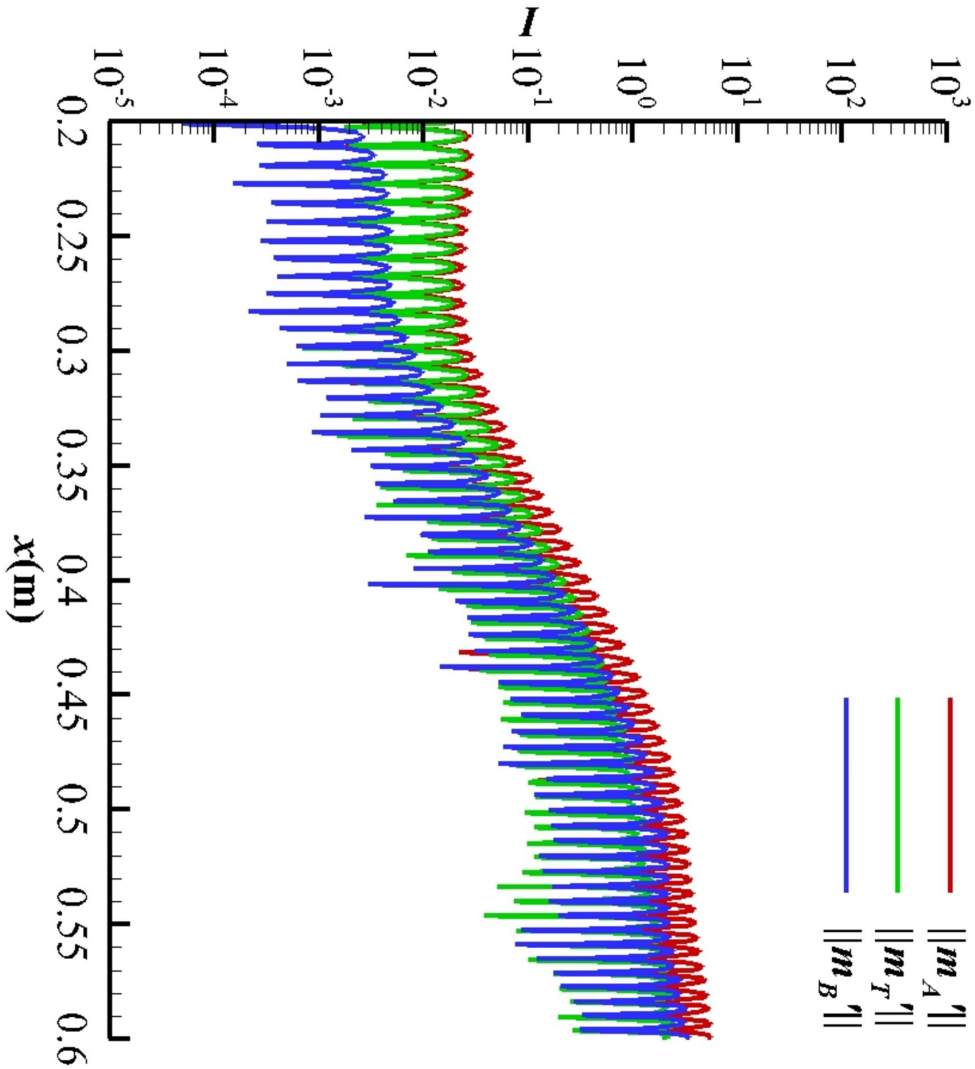

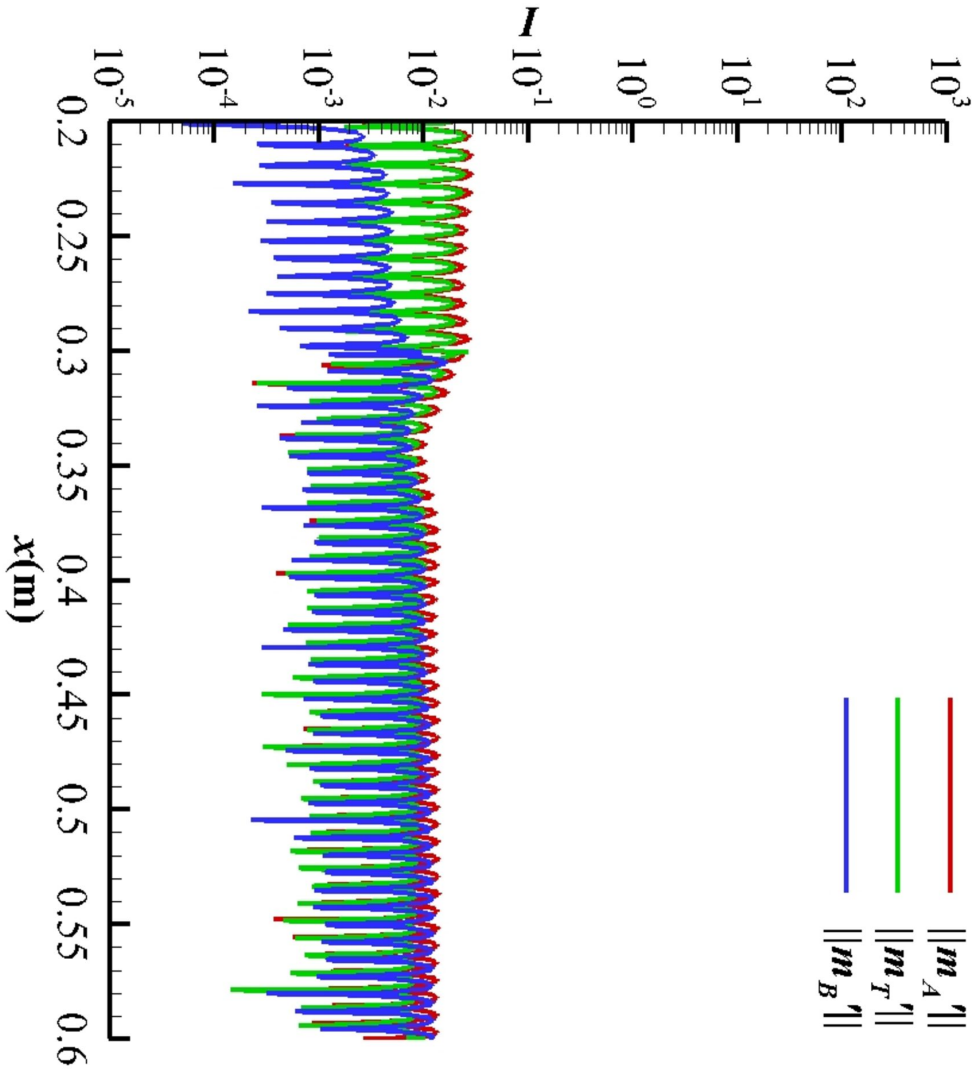

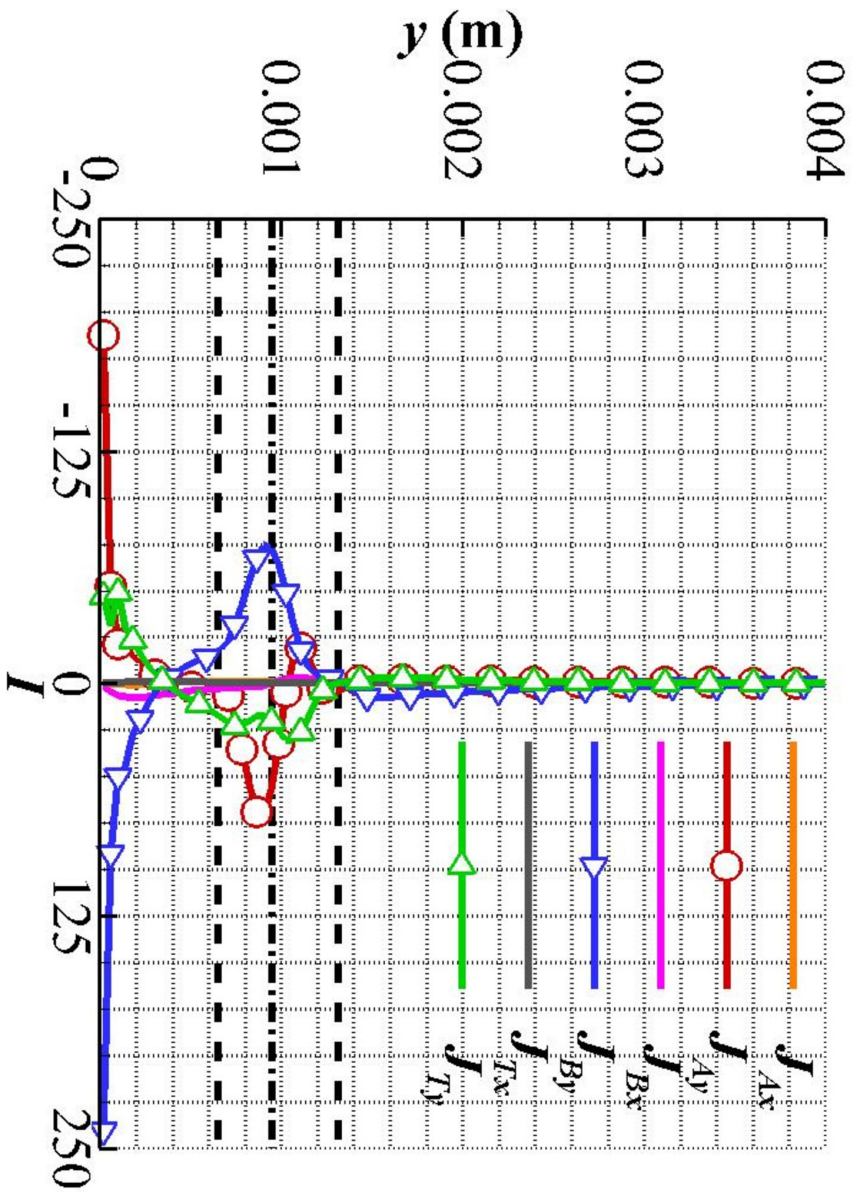

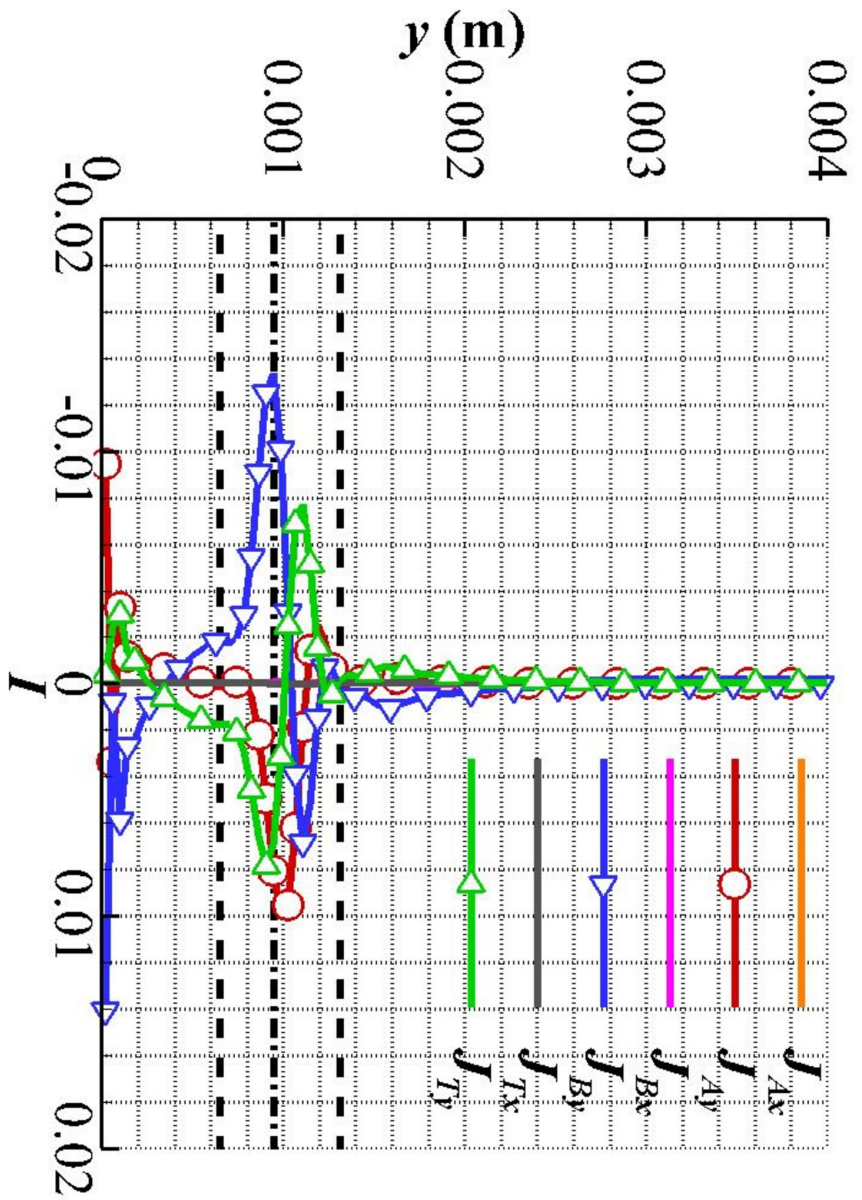

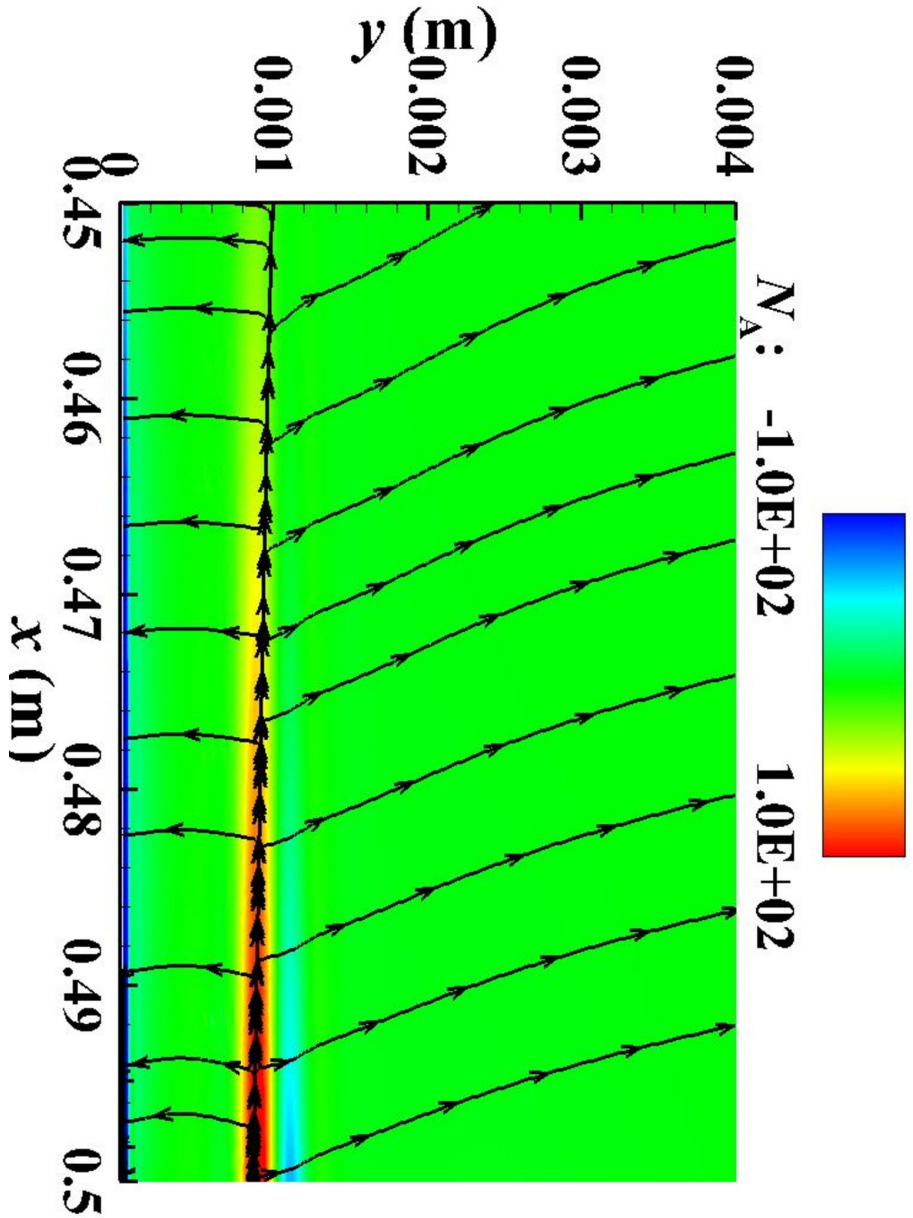

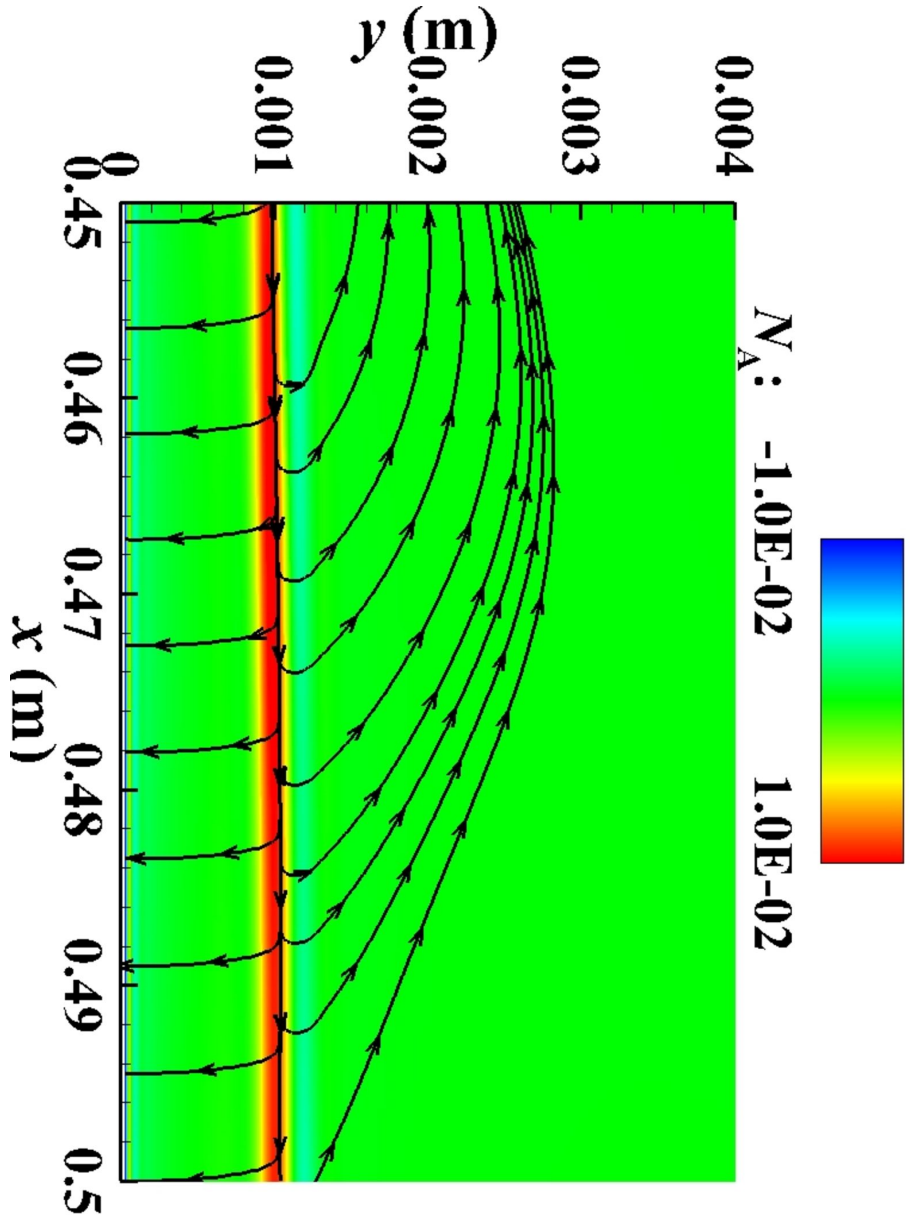

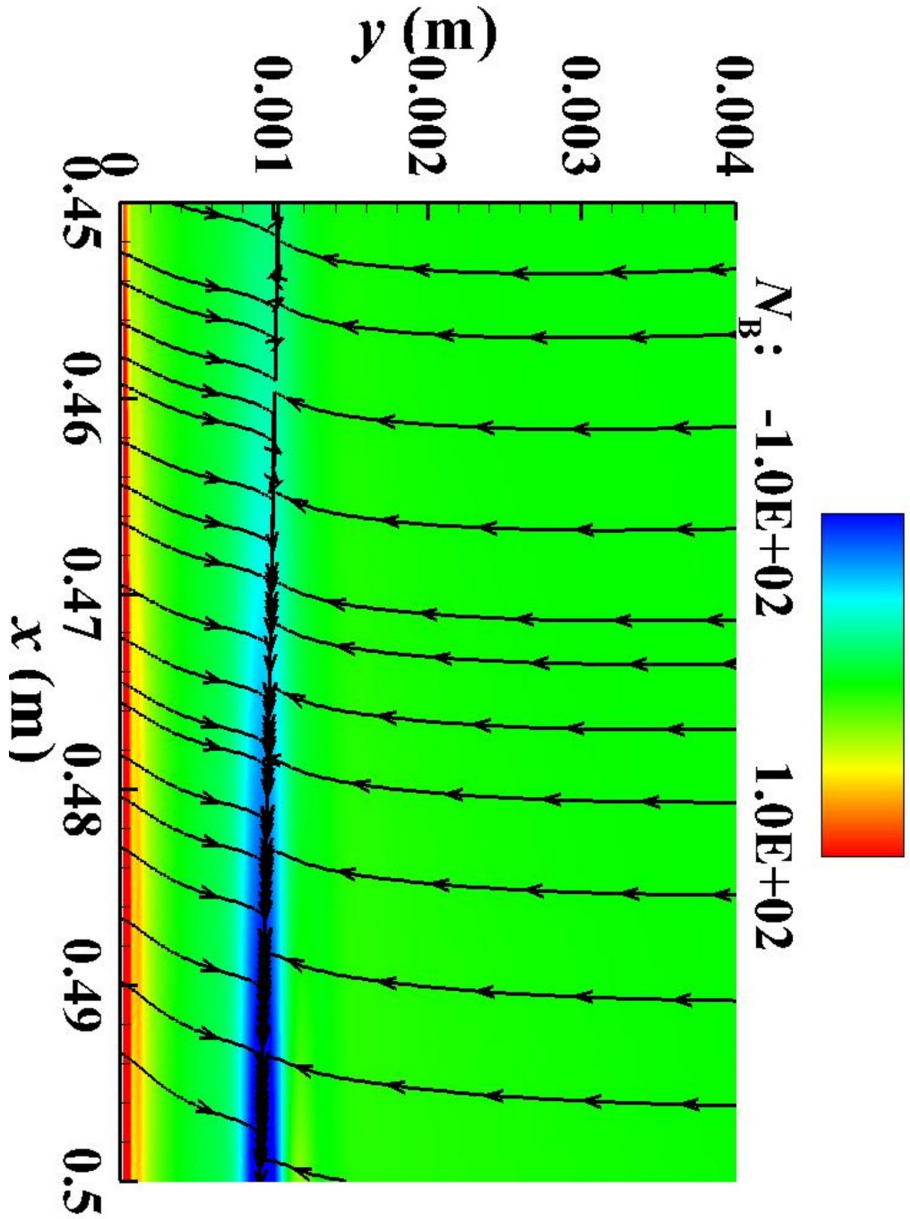

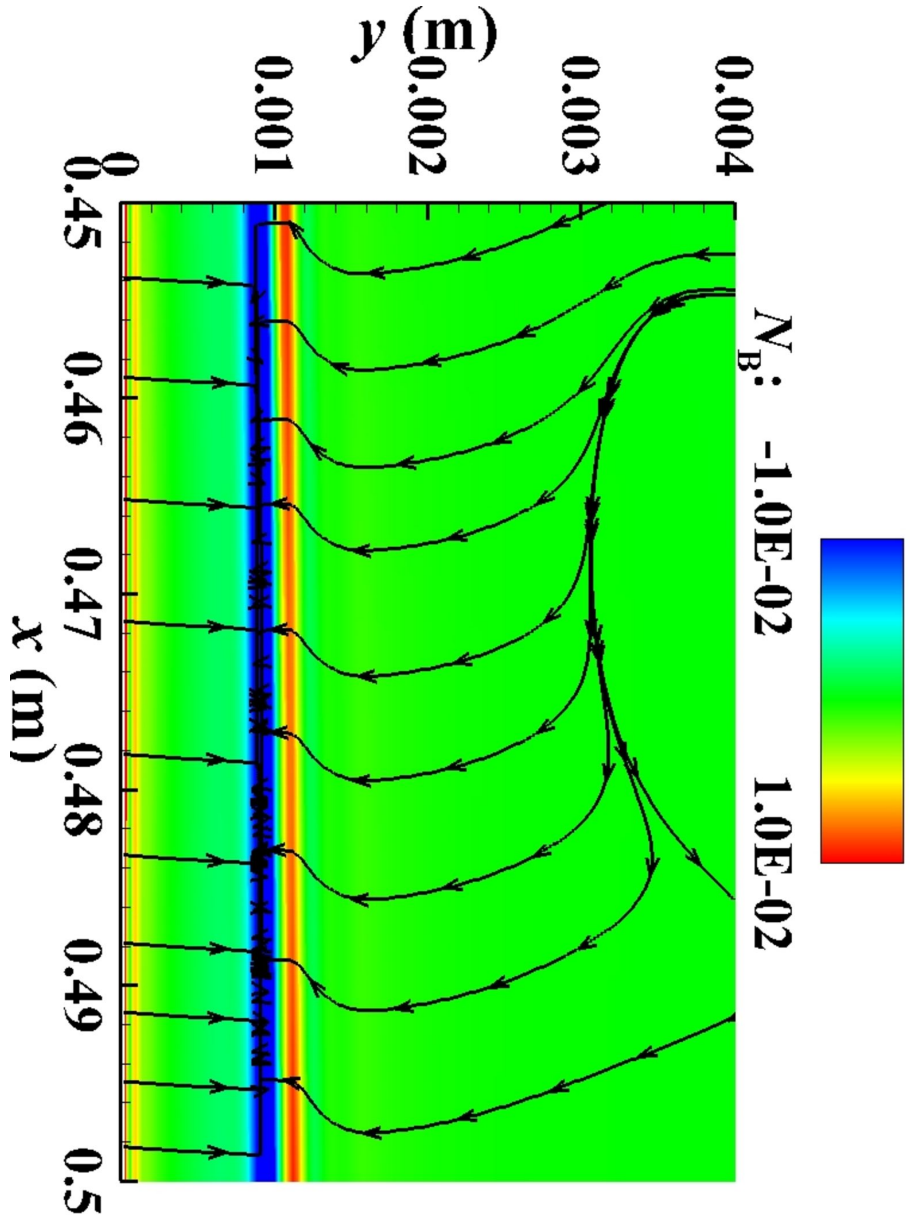

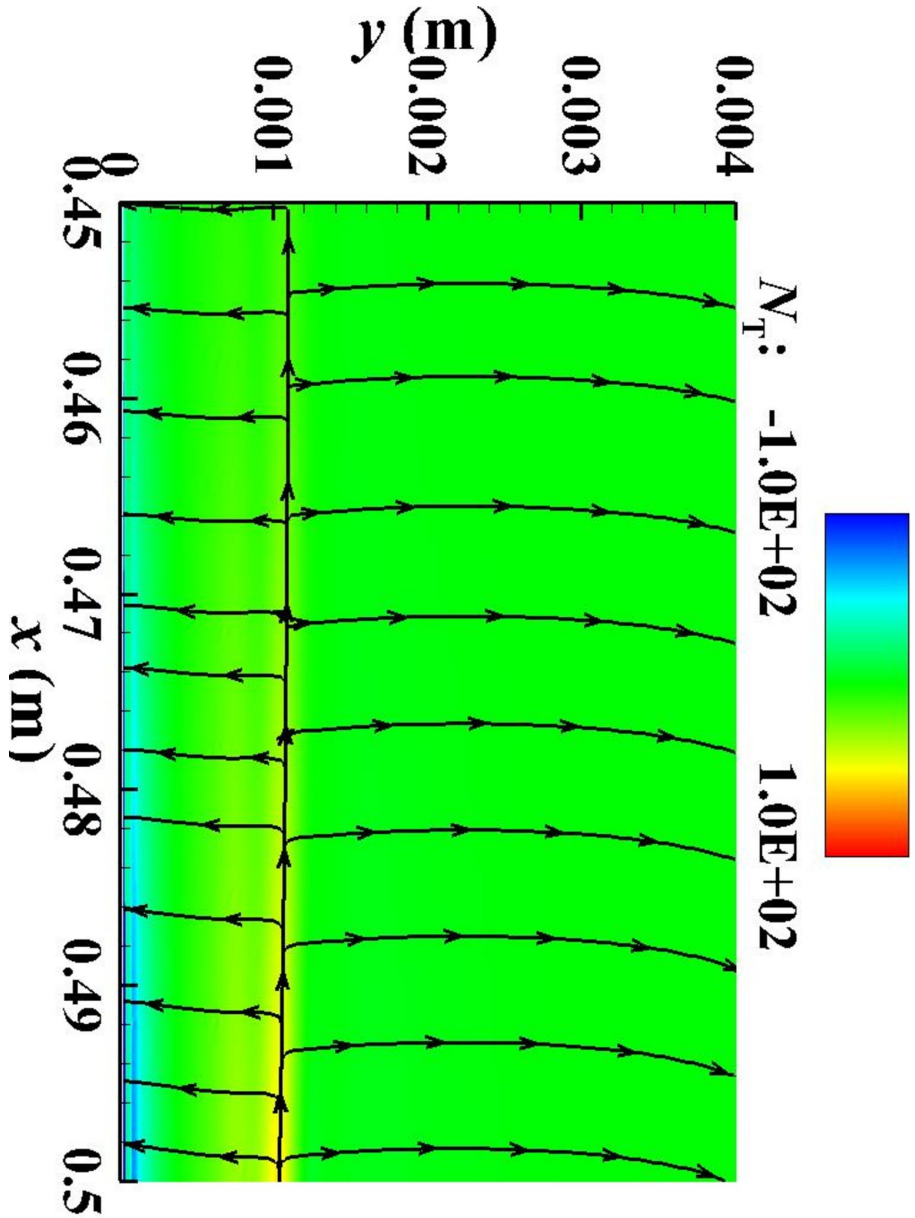

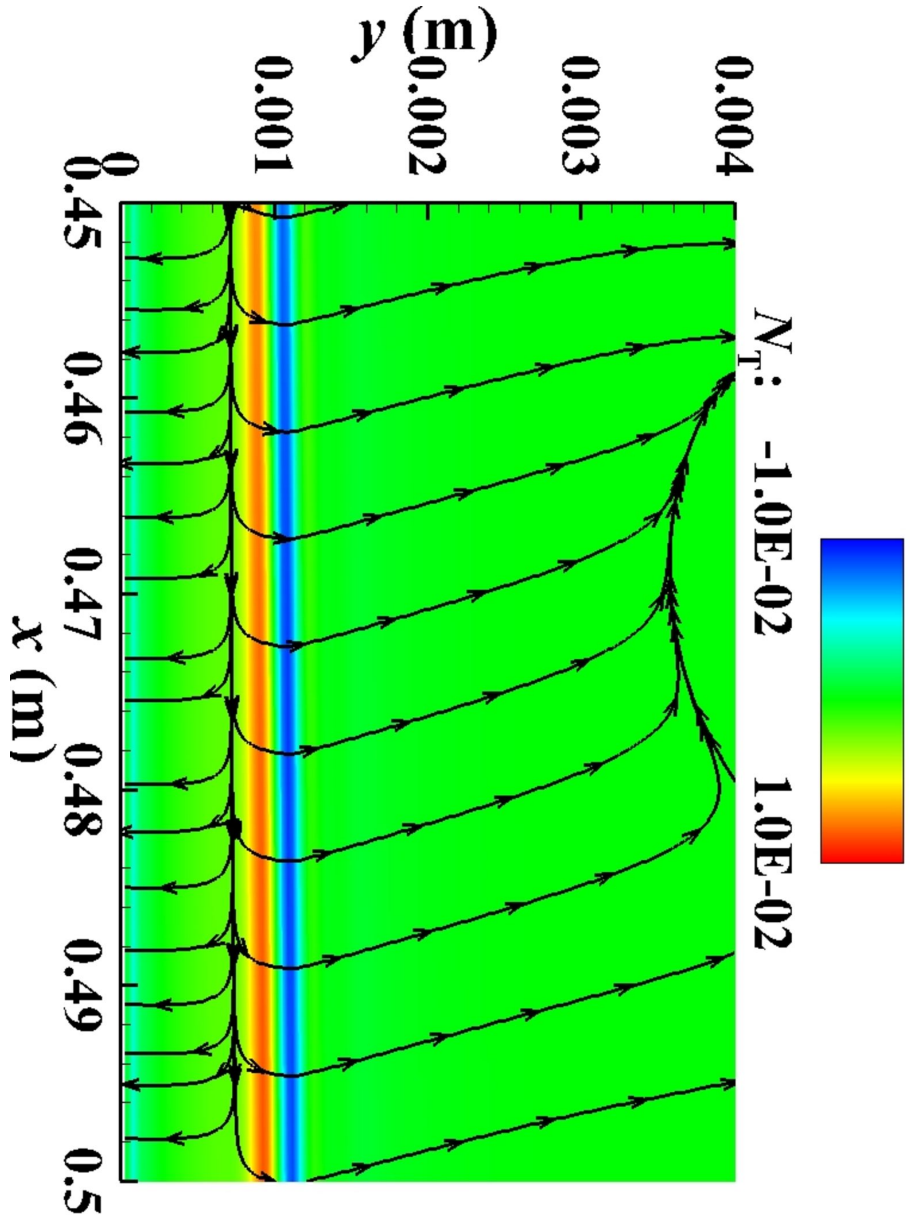

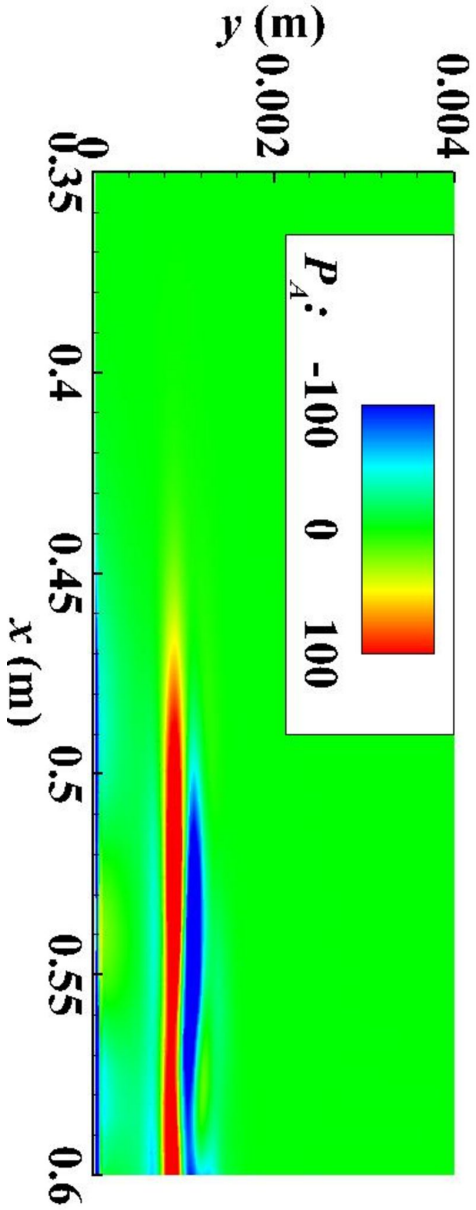

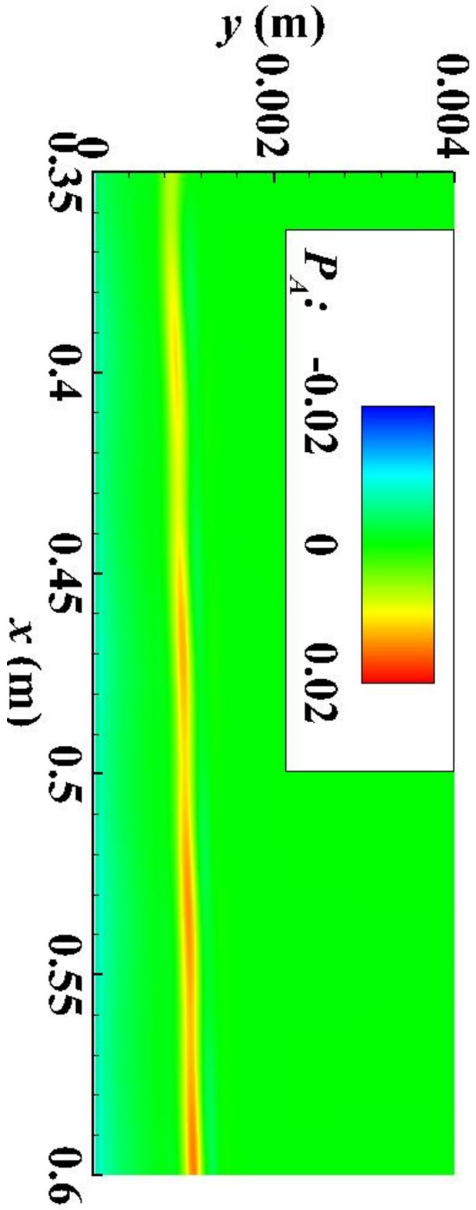

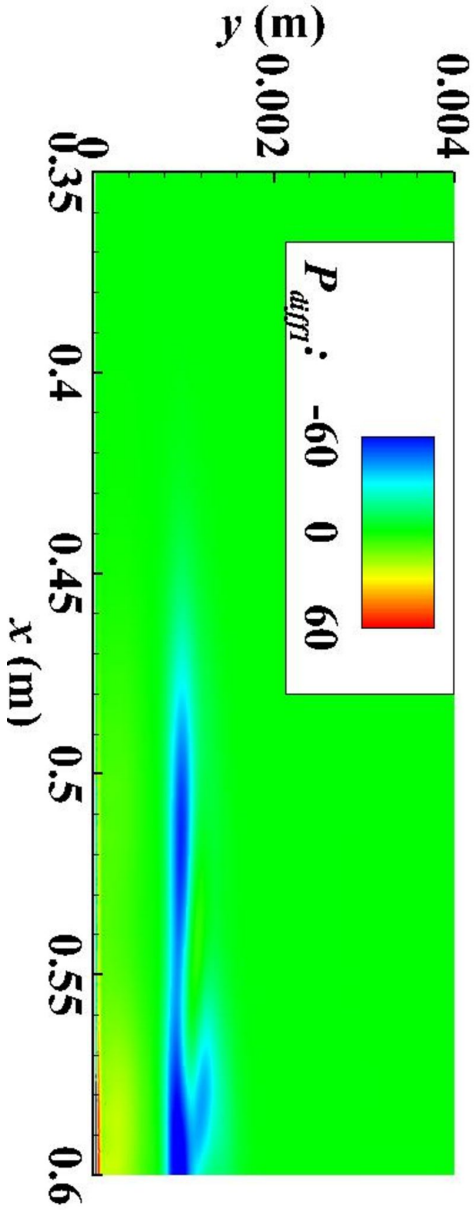

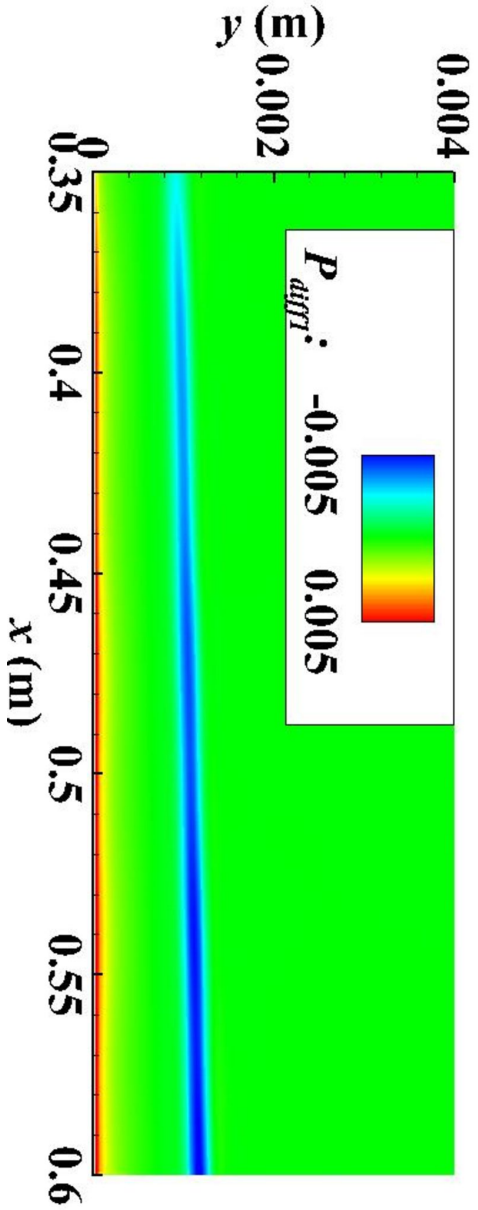

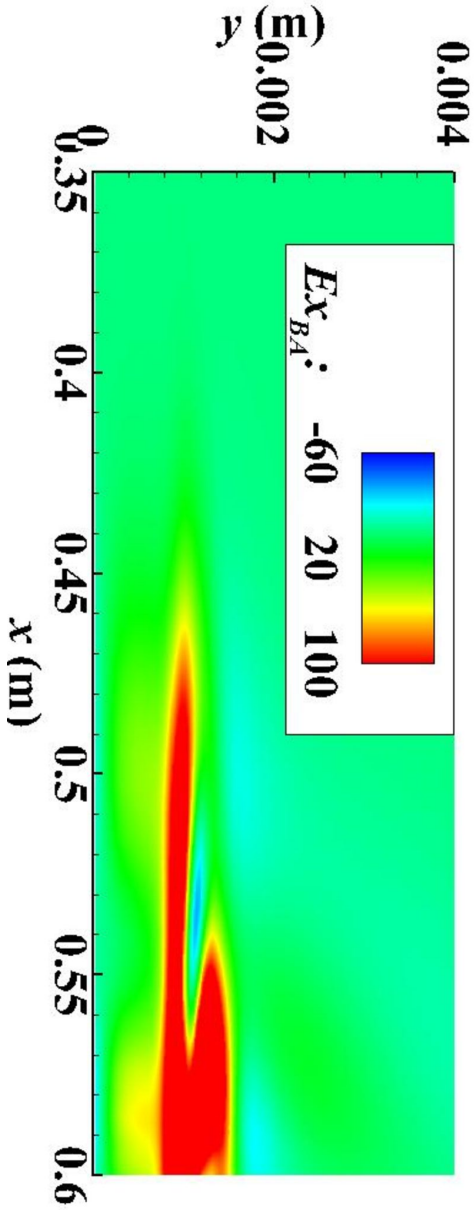

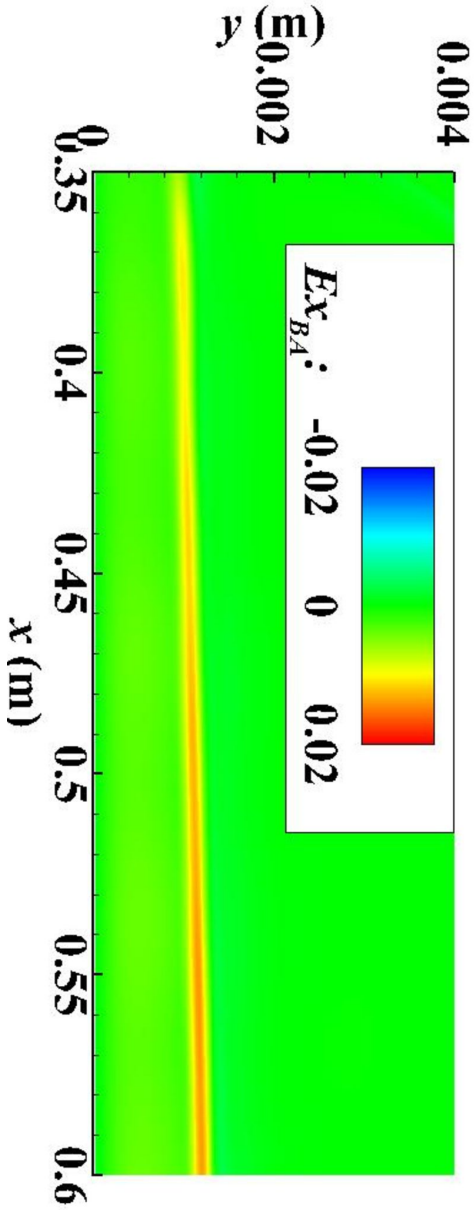

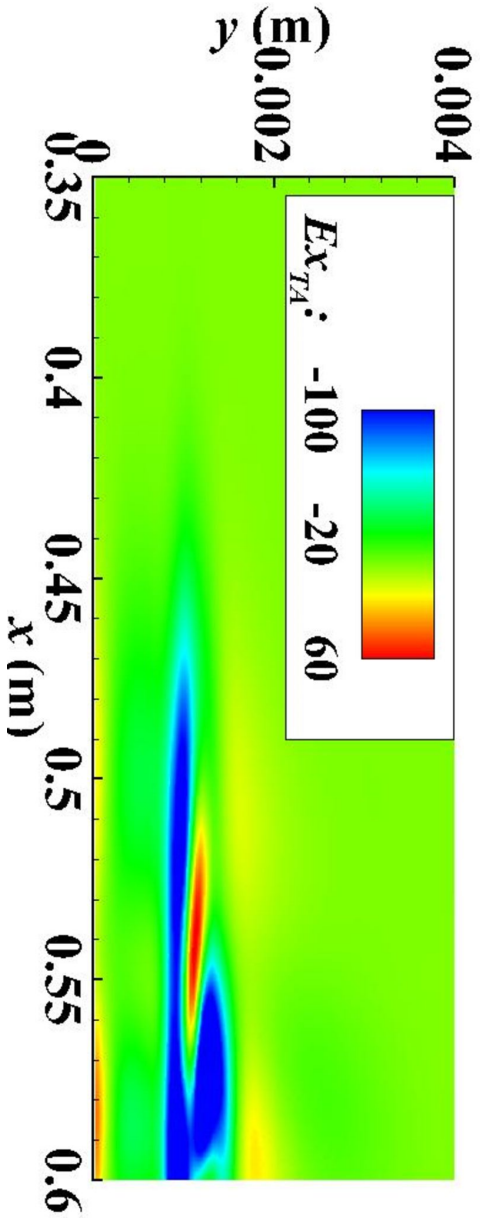

PLEASE CITE THIS ARTICLE AS DOI: 10.1063/5.0048313